Journal of Computational Physics 228 (2009) 661–686

Contents lists available at ScienceDirect

Journal of Computational Physics

journal homepage: www.elsevier.com/locate/jcp

Development of a dispersively accurate conservative level set scheme for capturing interface in two-phase flows

Tony W.H. Sheu *, C.H. Yu, P.H. Chiu

Department of Engineering Science and Ocean Engineering, National Taiwan University, No. 1, Section 4, Roosevelt Road, Taipei 106, Taiwan, ROC

ARTICLE INFO

Article history:
Received 10 July 2007
Received in revised form 7 July 2008
Accepted 22 September 2008
Available online 1 November 2008

Keywords:
Interface capturing
Conservative level set method
Contact discontinuity oscillations
Dispersion-relation-preserving

ABSTRACT

A two-step interface capturing scheme, implemented within the framework of conservative level set method, is developed in this study to simulate the gas/water two-phase fluid flow. In addition to solving the pure advection equation, which is used to advect the level set function for tracking interface, both nonlinear and stabilized features are taken into account for the level set function so that a sharply varying interface can be stably predicted. To preserve the conservative property, the mapping given by $\underline{\xi} = \underline{x} - \underline{u}t$ is performed between two coordinates $\underline{x}$ and $\underline{\xi}$ for the advection–diffusion equation in a flow field with velocity $\underline{u}$. To capture the interface, the flux term capable of compressing the level set contours is also adopted in the construction of linear inviscid Burgers' equation, which is indispensable in the level set method. To resolve the physically sharp interface without incurring contact discontinuity oscillations, a damping term which is nonlinear in terms of the level set function and can render an adequate artificial diffusion to stabilize the contact surface is added into the reinitialization step in the modified level set method. For accurately predicting the level set function, the advection scheme for solving the linear inviscid Burgers' equation in the advection step of the modified level set method is developed to accommodate the true dispersion relation. The solution computed from the resulting two-dimensional dispersion-relation-preserving advection scheme can minimize the phase error. Less artificial damping is needed to damp the oscillations in the vicinity of contact surface and the interface can be less numerically smeared. For the sake of programming simplicity, the incompressible two-phase flow will be discretized in non-staggered grids without incurring checkerboard oscillations by the developed explicit compact scheme for the approximation of pressure gradient terms. For the verification of the proposed two-dimensional dispersion-relation-preserving scheme and the non-staggered incompressible flow solver, three benchmark problems have been chosen in this study. The proposed conservative level set method for capturing the interface in incompressible fluid flows is also verified by solving the dam-break, bubble rising in water, droplet falling in water and Rayleigh–Taylor instability problems. Good agreements with the referenced solutions are demonstrated for all the four investigated problems.

© 2008 Elsevier Inc. All rights reserved.

1. Introduction

Many problems of practical importance and scientific significance involve tracking of interface between different phases, where surface tension needs to be taken into account. These surface evolving problems include, for example, etching, deposition, lithography development in microfabrication processes [1]. Studies of the phenomena related to air–water interaction

* Corresponding author. Tel.: +886 2 33665746; fax: +886 2 23929885.
E-mail address: twhsheu@ntu.edu.tw (T.W.H. Sheu).

0021-9991/$ - see front matter © 2008 Elsevier Inc. All rights reserved.
doi:10.1016/j.jcp.2008.09.032

dynamics, breaking surface wave, solidification-melt dynamics, combustion, two-phase flow, reacting flow and flow-structure interactions fall into the framework involving a temporal surface advancement due to complex motion under different physical effects. The necessity of capturing the time–evolving interface with a sharply varying topology and a large change in front propagation speed makes the prediction of differential equations governing the respective two-phase flow an even challenging topic. In this study, we will consider the dam-break problem and investigate the fluid motions due to a rising air bubble in water, a droplet falling in water and Rayleigh–Taylor instability. Our attention will be concentrated on the development of incompressible flow algorithm, which can be applied to predict the air/water interface accurately with/without surface tension being taken into account in the prediction of surface advancement.

The most common incompressible flow algorithms that have been applied to track the air/water interfaces include vortex method [2], boundary integral method [3], volume of fluid (VOF) method [4], front tracking method [5] and phase field method [6–8]. One can also combine the level set method with the projection method to avoid an explicit tracking of interface [9]. There exist advantages and disadvantages for these interface capturing methods and it is difficult to assert which method is generally superior. Since the success of employing a particular interface capturing method depends on the problem under consideration and the available computing resource, it is fair to say that there may exist a class of problems for which one method can perform better than the other [10]. If surface tension needs to be considered in the simulation of incompressible two-phase flows, the volume of fluid method and the level set method are most commonly referred to.

The VOF method has the advantage of conserving the volume of each fluid phase exactly [11]. The interface in VOF methods is normally represented by a color function, defined as the fraction of the volume within each cell of one of the fluids, in a discontinuous fashion. Such a discontinuity can make the simulation of an evolving interface very difficult. In fact, no advection scheme for the VOF methods can offer an accuracy order larger than two [12]. The interface in level set methods can, on the other hand, be defined by the zero contour of a continuous signed distance function.

Subsequent to the pioneering work of Osher and Sethian [13], much progress has been made to construct various level set formulations, which have been applied to solve a large variety of problems that involve moving interfaces. Some application areas include the simulation of surface, flame propagation, shape reconstruction, image processing and crystal growth. Due to the smooth nature of the level set function across the interface, the interface and its curvature can be easily transported and accurately calculated, respectively. To retain the level set function, a signed distance function and a reinitialization procedure are normally required in the traditional level set method. The drawback is due, however, to the violation of geometric conservative law (GCL) [14,15] to preserve the volume as time is marched. In each time step, a small amount of mass may be lost or gained. As time evolves, these negligibly small errors may be accumulated to a large value and may, finally, break down the incompressible constraint condition. A modified level set method with the built-in conservative (or area-preserving in the incompressible flow simulations) property will be developed in this study to preserve the mass [12,16]. Description of the ideas about the level set method can be found in the books of Osher and Fedkiw [17] and Sethian [18].

The outline of this paper is as follows: In Section 2, the differential equations governing the motion of two fluids will be presented along with the transport equations for the fluid viscosity and density. Section 3 describes the two-step conservative level set method, which involves a nonlinear transport equation. In Section 4, the truly two-dimensional dispersion-relation-preserving advection scheme will be presented to dispersively more accurate advect the front of interface. Regularized incompressible flow solver, which is implemented in non-staggered grids, will be presented in Section 5 for solving the working primitive variables explicitly. Section 6 is presented to validate the employed analysis code by solving one linear inviscid Burgers' equation with a sharply varying initial condition and one Navier–Stokes problem with the benchmark solution for the carrier fluid flow. Section 7 is addressed to investigate the dam-break, bubble rising, droplet falling and Rayleigh–Taylor instability problems. Finally, we will draw some conclusions in Section 8.

2. Governing equations

Of the two immiscible fluids under current investigation, one is known as a liquid and the other is a gas. Both of them are considered to be incompressible. The resulting equations of motion for the gas and liquid fluids in a gravitational vector field $\underline{g}$ can be represented by the incompressible Navier–Stokes equations given below:

$$\frac{D\underline{u}}{Dt} = \frac{1}{\rho}(-\nabla p + \nabla \cdot (2\mu \underline{\underline{\mathbf{D}}}) - \underline{T} + \rho \underline{g}), \tag{1}$$

$$\nabla \cdot \underline{u} = 0, \tag{2}$$

where $\frac{D\underline{u}}{Dt}\left(\equiv \frac{\partial \underline{u}}{\partial t} + (\underline{u} \cdot \nabla)\underline{u}\right)$ represents the material derivative of the fluid velocity vector $\underline{u}$. The physical properties ρ and μ shown in Eq. (1) represent the fluid density and the fluid viscosity, respectively. Both of them are functions of the time and space, implying that $\rho = \rho(\underline{x}, t)$ and $\mu = \mu(\underline{x}, t)$. The tensor $\underline{\underline{\mathbf{D}}}$ shown above denotes the rate of deformation, with the components denoted by $D_{ij} = \frac{1}{2}(u_{i,j} + u_{j,i})$. In addition to the stress tensor given by $-p\underline{\underline{\mathbf{I}}} + 2\mu\underline{\underline{\mathbf{D}}}$, where $\underline{\underline{\mathbf{I}}}$ is the identity matrix, the other source term capable of resulting in flow acceleration is the surface tension $\underline{T}$ concentrated solely on the two-fluid interface, which is denoted by the phase field function Φ.

In this study, the surface tension will be modified as the body force and is applied at the interface. In other words, the surface tension per unit interfacial area is given by

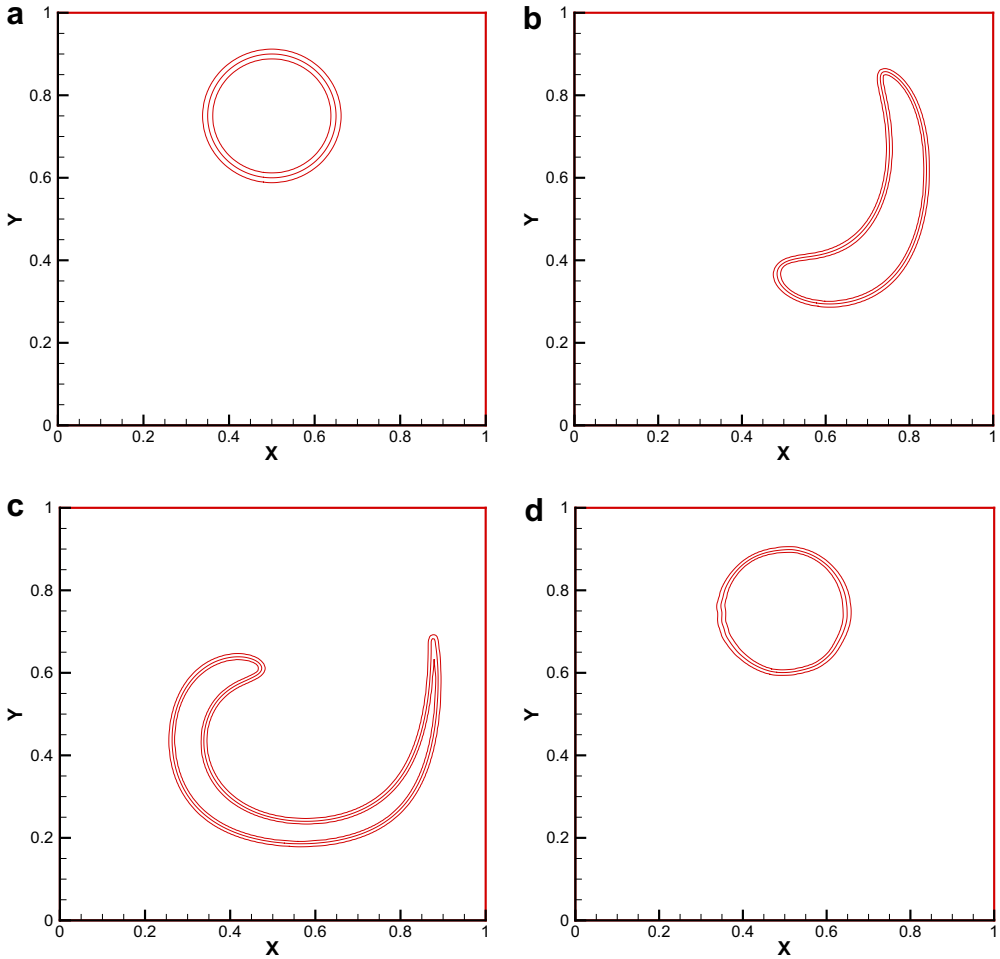

Fig. 1. The interfaces plotted in a domain of 257×257 grids were predicted at (a) $t = 0$, (b) $t = 0.5$, (c) $t = 1$, (d) $t = 2$. The contours for the inner, middle and outer lines represent $\Phi = 0.95, 0.5$ and 0.05, respectively.

$$\underline{T} = \sigma\kappa\underline{n}. \tag{3}$$

In the above, σ is denoted as the surface tension coefficient, κ is the curvature of the interface and the unit outward normal vector $\underline{n}$ along the interface is normally pointed to the surrounding liquid. One can express the normal and curvature of an interface in terms of Φ as $\underline{n} = \frac{\nabla\Phi}{|\nabla\Phi|}$ and $\kappa = \nabla \cdot \frac{\nabla\Phi}{|\nabla\Phi|}$. This clearly explains why the Navier–Stokes equations need to be formulated within the framework of level set method. In this study, the curvature term is approximated by the second-order accurate central scheme as $\left(\nabla \cdot \frac{\nabla\Phi}{|\nabla\Phi|}\right)_{i,j} = \frac{1}{2\Delta x}\left(\frac{(\Phi_x)_{i+1,j}}{|(\nabla\Phi)_{i+1,j}|} - \frac{(\Phi_x)_{i-1,j}}{|(\nabla\Phi)_{i-1,j}|}\right) + \frac{1}{2\Delta y}\left(\frac{(\Phi_y)_{i,j+1}}{|(\nabla\Phi)_{i,j+1}|} - \frac{(\Phi_y)_{i,j-1}}{|(\nabla\Phi)_{i,j-1}|}\right)$, where $(\nabla\Phi)_{i,j} = (\Phi_x)_{i,j}\tilde{i} + (\Phi_y)_{i,j}\tilde{j} = \frac{\Phi_{i+1,j}-\Phi_{i-1,j}}{2\Delta x}\tilde{i} + \frac{\Phi_{i,j+1}-\Phi_{i,j-1}}{2\Delta y}\tilde{j}$ and $|(\nabla\Phi)_{i,j}| = \sqrt{(\Phi_x)_{i,j}^2 + (\Phi_y)_{i,j}^2}$.

The above equations cast in the dimensional form will be normalized for the sake of general application. Taking $u_r, l_r, t_r, \rho_r g l_r, \rho_r, \mu_r$ as the referenced values for the respective velocity, length, time, pressure, density and viscosity, the normalized (or dimensionless) continuity equation remains unchanged. The momentum equation after the proposed non-dimensionalization can be formulated as

$$\underline{u}_t + (\underline{u} \cdot \nabla)\underline{u} = \frac{1}{\rho}\left(-\nabla p + \frac{1}{Re}\nabla \cdot (2\mu\underline{\underline{\mathbf{D}}}) - \frac{1}{We}\kappa(\Phi)\nabla\Phi\right) + \frac{1}{Fr^2}\underline{e}_g, \tag{4}$$

where $\underline{e}_g$ is the unit gravitational direction vector and the Reynolds number is given by $Re = \frac{\rho_r u_r l_r}{\mu_r}$. Another characteristic parameter We is known as the Weber number, which is defined as $We = \frac{\rho_r u_r^2 l_r}{\sigma}$. Both density and viscosity will be smoothly approximated by $\rho = \rho_1 + (\rho_2 - \rho_1)\Phi$ and $\mu = \mu_1 + (\mu_2 - \mu_1)\Phi$, where ρ_i and $\mu_i (i = 1, 2)$ are the dimensionless densities and viscosities of the two investigated fluids, respectively. As for Φ it will be defined later in Section 3.

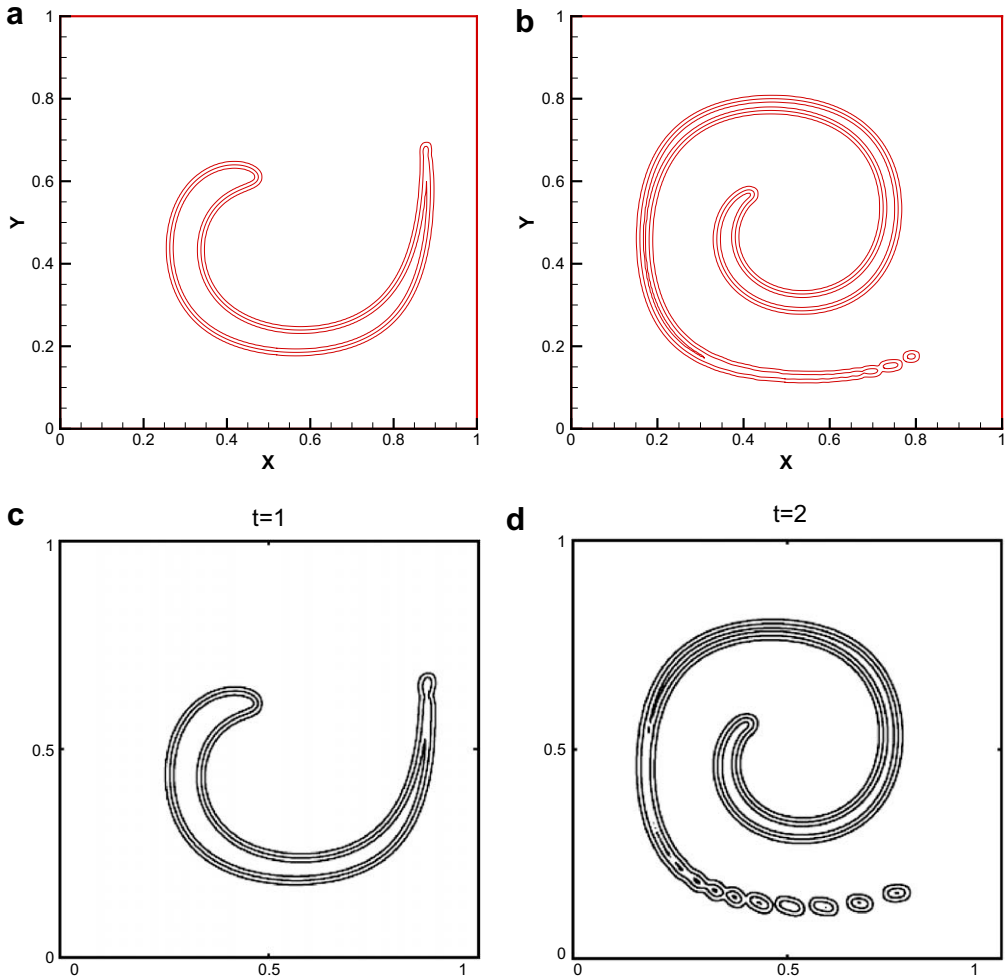

Fig. 2. The interfaces plotted in a domain of 257×257 grids were predicted at (a) $t = 1.0$, (b) $t = 2.0$, (c) $t = 1.0$ [12], (d) $t = 2.0$ [12]. The contours for the inner, middle and outer lines represent $\Phi = 0.95, 0.5$ and 0.05, respectively.

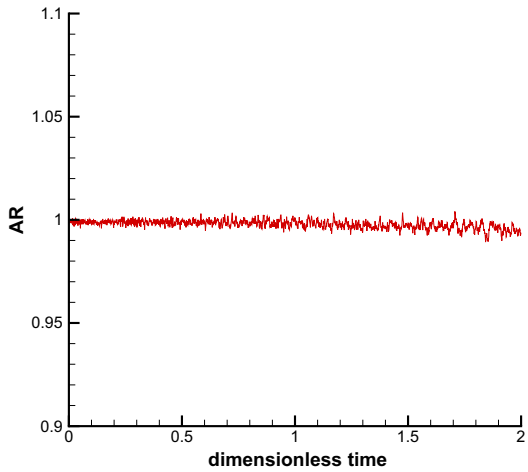

Fig. 3. The plot of the predicted area ratio (AR) against the dimensionless time for the problem given in [12]. Note that AR is defined as $\mathrm{AR} = \frac{\int \Phi(x,y;\ \text{for}\ 0.5 \leqslant \Phi \leqslant 1, t) dA}{\int \Phi(x,y;\ \text{for}\ 0.5 \leqslant \Phi \leqslant 1, t=0) dA}$.

3. Two-step interface capturing level set method

For the investigated two immiscible fluids, the physical properties ρ and μ are assumed to be constant in their respective phases in the sense that $\frac{D\rho}{Dt} = \frac{D\mu}{Dt} = 0$. There exists, however, a jump across the interface. As a result, the equations governing the distributions of density and viscosity depend on the fluid velocity $\underline{u}$ as follows:

$$\rho_t + (\underline{u} \cdot \nabla)\rho = 0, \tag{5}$$

$$\mu_t + (\underline{u} \cdot \nabla)\mu = 0. \tag{6}$$

Since ρ and μ may be changed sharply across the air/water interface, numerical simulation of the transport equations for ρ and μ, governed respectively by Eqs. (5) and (6), is computationally very challenging. The difficulty is attributed to the presence of contact discontinuities, which can incur unphysical oscillations. Such an academic difficulty has long been known also in the gas dynamics community when contact discontinuities are formed in a highly compressible gas flow. Since no rigorous theory can be applied to suppress this type of oscillations in the vicinity of multi-dimensional contact surfaces, we shall use the modified level set method of Olsson et al. [16] to capture the interface.

As the interface will be advected with the fluid, the interface separating the two fluids can be regarded as the evolution of Φ governed by $\frac{D\Phi}{Dt} = 0$ or by the linear inviscid Burgers' equation given by $\Phi_t + \nabla \cdot (\underline{u}\Phi) = 0$. In other words, the hyperbolic equation for Φ will be used to represent the contour level of Φ at interface in a way like an actual interface movement. Unlike ρ and μ, which are discontinuous across the interface, Φ will be made to be slightly smoothed to avoid the difficulty of dealing with the contact discontinuity when solving Eqs. (5) and (6). This implies that the jump of phase properties across the interface needs to be smoothed in order to avoid numerical instabilities near the interface [19]. Within the continuous framework, across the interface the Heaviside step function (or unit step function) for ρ and μ needs to be smoothed with a certain degree of smearing at the interface to render a smeared-out Heaviside function. For the sake of smoothly preserving the sharp front, the Heaviside step function approximated in a way given below will be employed to retain the interface as steep as possible

$$\Phi = \begin{cases} 0; & \text{if } |\underline{x}| > 3\bar{\mu}, \\ (1 + e^{\underline{x}/\bar{\mu}})^{-1}; & \text{if } -3\bar{\mu} \leqslant |\underline{x}| \leqslant 3\bar{\mu}, \\ 1; & \text{if } |\underline{x}| < -3\bar{\mu}, \end{cases} \tag{7}$$

Table 1
The predicted L_1-error norms and the rates of convergence at $t = 2T(T = 0.5)$ in the five chosen meshes, $\Delta t = \frac{1}{10.000}$ and $\bar{\mu} = \Delta x$. Note that at $t = 0.5$ the flow velocity was reversed.

No. of nodal points	L_1 error norms	Rates of convergence
61×61	4.126239265345434E–003	
101×101	1.379342840129760E–003	2.14507
141×141	5.954776782349826E–004	2.49649
181×181	2.947313760961025E–004	2.79848
221×221	1.753773477596643E–004	2.58695

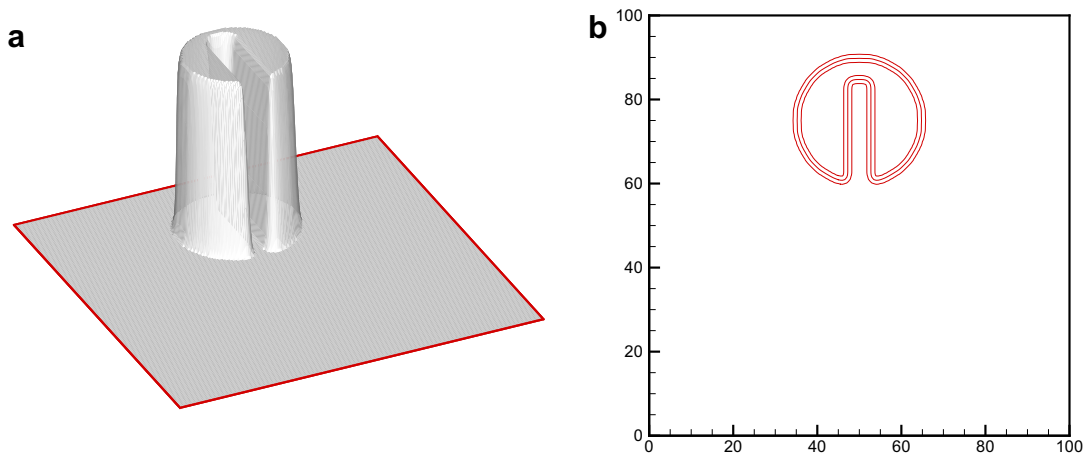

Fig. 4. The initial profile of Φ for the test problem given in Section 6.2.The diffusion coefficient is specified by $\bar{\mu} = \Delta x$. (a) three-dimensional view of the predicted solution; (b) cross sectional view of $\Phi = 0.05$ (outer), $\Phi = 0.5$ (middle), $\Phi = 0.95$ (inner) contour lines.

where $\underline{x}$ denotes the distance vector in space to the interface. As a result, ρ and μ can be smoothly distributed across the interface to prevent numerical instability arising from the contact surface when solving their transport equations. It is noted that the magnitude of Φ at the interface has been made to change rapidly from zero to one across the interface, at which the magnitude of Φ is 0.5 according to Eq. (7).

While level set methods can be applied to predict the topological change of interface present in compressible and incompressible two-phase flows, the relatively more accurate conventional level set methods are not conservative. This drawback is particularly severe in the simulation of incompressible two-phase flow problems. Any loss or gain in mass will incur physically erroneous results [20]. To improve mass conservation, several attempts with different underlying ideas have been made in the level set methods [12,21,22]. Given a smeared-out Heaviside function $\Phi(\underline{x}, t = 0)$ in a divergence-free velocity field, our goal is to develop a dispersively accurate method to advect Φ so as to preserve the initially prescribed smooth profile of $\Phi(\underline{x}, t = 0)$ and the solution $\Phi(\underline{x}, t)$ computed at the time $t = n\Delta t$. In mathematical description, the property given by $\int \Phi d\Omega$ (=constant) needs to be satisfied perfectly so as to render a conservative (or area-preserving) scheme. With the objective of maintaining a good conservation of area bounded interface, the employed advection scheme should also accommodate the good dispersive nature so as to be able to predict the non-oscillatory sharp interface.

We now turn to the subject of developing a method to advect the value of Φ so that it is conservative and can possess the sharp property. For an easier description of the interface capturing method, consider the following transport equation for the advection of Φ, subjected to an initial condition $\Phi_0(\underline{x}, t = 0)$, in a fluid with the velocity field $\underline{u} = (u, v)$

$$\Phi_t + \nabla \cdot (\underline{u}\Phi) = 0. \tag{8}$$

To retain the conservation property, given by $\int \Phi d\Omega$, all the time, it is desired to assure that $\Phi(\underline{x}, t) = \Phi(\underline{x} - \underline{u}\Delta t, t - \Delta t)$. In actual computation, any employed stable numerical scheme will introduce diffusion error that will more or less smear the predicted solution as time proceeds. Since in the linear differential system no mechanism can steepen the solution, development of another nonlinear equation for ψ, which is linearly related to the unknown field variable Φ, becomes a vital means to achieve the goal of interface capturing.

Within the framework of linear transformation between the independent variables, namely, $\underline{\xi} = \underline{x} - \underline{u}t$, to preserve the conservative property and for the dependent variables, namely, $\psi(\underline{\xi}, t) = 1 - 2\Phi(\underline{\xi}, t)$, the equation given below for ψ will be chosen to compress the solution [16]:

$$\psi_t + \frac{1}{2}\nabla(\psi^2) = \bar{\mu}\nabla^2\psi. \tag{9}$$

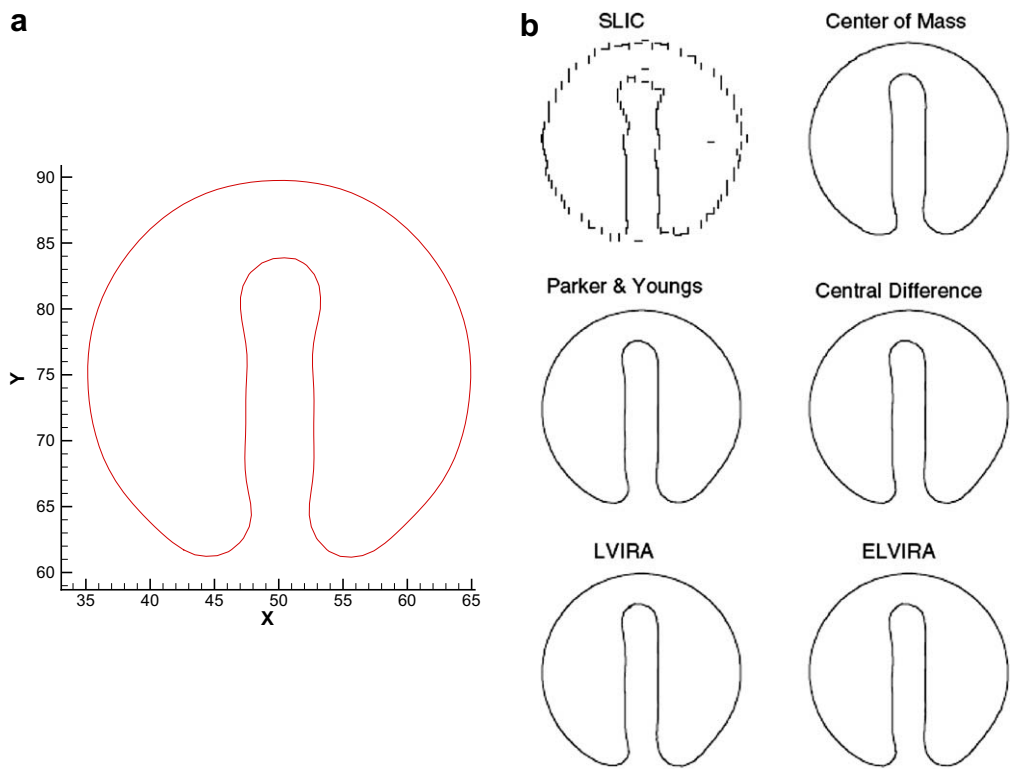

Fig. 5. (a) The predicted result using the current conservative level set method with 101×101 nodal points for the Zalesak's test problem; (b) The results shown in [29] for the operator split advection algorithm and the various interface reconstruction methods for the Zalesak's test problem.

The artificial damping coefficient (or artificial viscosity) $\bar{\mu}$ shown above needs to be prescribed with a small magnitude but it can retain the sharply varying interface. Given the nonlinear equation for ψ in Eq. (9), the stabilized advection of Φ across the interface along the direction normal to the interface can be expressed as follows by virtue of the above mentioned linear transformation between the coordinates $\underline{x}$ and $\underline{\xi}$ and the linear mapping between the solution variables Φ and ψ:

$$\Phi_t + \nabla \cdot (\underline{u}\Phi) = \nabla \cdot (-\Phi(1-\Phi)\underline{n} + \bar{\mu}\nabla \cdot (\nabla\Phi)), \tag{10}$$

where $\underline{n} = \nabla\Phi/|\nabla\Phi|$ represents the unit normal vector of the gas/water interface. Note that the transport equation for the level set function can no longer be simply governed by the linear inviscid Burgers' Eq. (8), which is normally employed in the conventional level set method. The source term shown in the right hand side of Eq. (10) makes the governing equation for the level set function to be nonlinear. As a result, the transport of Φ in a nonlinear way by virtue of Eq. (10) may help to achieve the goal of compressing the solution profile. The predicted interface can therefore be sharp in the course of numerical simulation.

Calculation of the inhomogeneous nonlinear viscous Burgers' Eq. (10), which can artificially compress the interface profile, will be split into two steps for solving the respective linear inviscid Burgers' equation and the nonlinear viscous Burgers' equation. The reason is that the working equation employed in each fractional step resembles the frequently investigated model equation. Within each time step, Φ will be firstly computed from $\Phi_t + \nabla \cdot (\underline{u}\Phi) = 0$, which is the equation normally employed in the traditional level set method to advect Φ. The computed linear inviscid Burgers' solution for Φ is then employed as the initial solution to solve the following nonlinear equation for the sake of stabilization and compression of Φ across the interface:

$$\Phi_\tau + \nabla \cdot (\Phi(1-\Phi)\underline{n}) = \bar{\mu}\nabla \cdot (\nabla\Phi). \tag{11}$$

Note that $\Phi(1-\Phi)\underline{n}$ in the left hand side of the above equation can be regarded as the compressive flux term. Due to its nonlinear nature, high resolution of the contact surface can be possibly maintained. Furthermore, the artificial damping term introduced into the formulation to avoid numerical oscillations due to discontinuities present at the interface is also nonlinear with respect to Φ. Calculation of Eq. (11) will be repeated until the steady-state solution is obtained. Owing to the current use of explicit scheme, solution will be calculated subject to the stability constraint condition given by $\Delta\tau \leqslant C\frac{(\Delta x)^2}{\bar{\mu}}$, where $C = \frac{1}{4}$. In this study, the time step is chosen to be $\frac{1}{10}\frac{(\Delta x)^2}{\bar{\mu}}$. In practice, only few time steps are sufficient for all the computations carried out in this study.

Employment of the two-step solution algorithm can make the currently employed level set method to be conservative. In other words, Eq. (11) can be considered as the correction equation for the conservative level set method to compress the level set contour near the interface. Note that stabilization and compression of the solution are both essential to stably preserve the sharp air/water interface while Eq. (8) is served to assure the conservative property. There remains to determine the numerically introduced artificial viscosity $\bar{\mu}$, which needs to be prescribed for the stabilization sake. The magnitude of $\bar{\mu}$ shown in Eq. (11) accounts for the thickness of the interface between $\Phi = 0$ and $\Phi = 1$. In what follows, $\bar{\mu}$ will be chosen as Δx in all calculations.

4. Dispersively accurate multi-dimensional advection scheme

In the numerical prediction of multi-dimensional flow problems, which involve interface that separates the fluids of different physical properties, it is essential to suppress oscillations, predicted near the contact surface, within a distance as short as possible. Since no Eulerian scheme, to the best of authors' knowledge, can be employed to eliminate the erroneous oscillations near the contact surface, the artificial viscosity $\bar{\mu}$ shown in Eq. (11) must be a non-zero positive value for the stabilization purpose. An improper specification of $\bar{\mu}$ may over-diffuse the profile of Φ and a sharp capturing of interface is impossible. Hence, it is important to alleviate the computational difficulty in association with the approximation of Eq. (11). One trivial means to achieve the above goal is to eliminate the origin of oscillations, which is known to be the erroneously introduced dispersive error. For this reason, we are motivated to develop a dispersively accurate two-dimensional transport scheme for the approximation of the first-order derivative terms shown in Eqs. (4) and (8). The artificial viscosity, introduced to damp the oscillations in the vicinity of air/water interface, can be minimized. The physical interface can therefore be well captured all the time. In the following, the advection scheme which can preserve the dispersion relations for the first-order derivative terms will be briefly described.

The underlying idea of approximating the first-order spatial derivative terms shown in Eq. (4) for $\frac{\partial u}{\partial x}, \frac{\partial u}{\partial y}, \frac{\partial v}{\partial x}, \frac{\partial v}{\partial y}$ and in (8) for $\frac{\partial}{\partial x}(u\Phi), \frac{\partial}{\partial y}(v\Phi)$ is to preserve their dispersion relations, which stand for the relation between the angular frequency of the wave and the wavenumber of the first-order derivative term, so that the convective instability can be effectively eliminated. For easily describing the way of approximating these first-order derivative terms, a scheme accommodating the dispersion-relation-preserving property for these derivative terms denoted by F_x and F_y will be developed under $\Delta x = \Delta y = h$. In the case of $u > 0$, F_x at a nodal point (i,j) can be approximated by $\frac{F_{i+1/2,j} - F_{i-1/2,j}}{\Delta x}$, where $(u\Phi)_{i+1/2,j}$ (or $F_{i+1/2,j}$) and $(u\Phi)_{i-1/2,j}$ (or $F_{i-1/2,j}$) are weighted by their adjacent nodal values. Note that this control-volume approximation is an aid to achieve area preservation. The resulting F_x at an interior node (i,j) can be expressed as follows in the 12-point stencil grid

$$\begin{aligned} F_x(x,y) \simeq \frac{1}{h}(&a_1F_{i-1,j-1} + a_2F_{i,j-1} + a_3F_{i+1,j-1} + a_4F_{i-1,j} + a_5F_{i,j} + a_6F_{i+1,j} + a_7F_{i-1,j+1} + a_8F_{i,j+1} + a_9F_{i+1,j+1} + a_{10}F_{i,j-2} \\ &+ a_{11}F_{i,j+2} + a_{12}F_{i-2,j}). \end{aligned} \tag{12}$$

Substitution of Taylor series expansions for $F_{i\pm1,j}$, $F_{i_2,j}$, $F_{i,j\pm1}$, $F_{i,j\pm2}$, $F_{i\pm1,j\pm1}$ into the above equation, we are led to derive the resulting modified equation for F_x. The derivation is followed by eliminating the eleven leading error terms so as to be able to derive a system of eleven algebraic equations. One more equation needs to be derived for uniquely determining the values of $a_1 \sim a_{12}$ shown in Eq. (12).

It is essential that the dispersion relation be retained to enable an effective suppression of the convective oscillations, in particular, in the prevailing convection case [23]. It is desired that the right hand side of Eq. (12) becomes nearly the same, by Fourier transform in space, as the original derivative term shown in the left hand side. The Fourier transform and its inverse for $F(x,y)$ are defined respectively as follows:

$$\widetilde{F}(\alpha,\beta) = \frac{1}{(2\pi)^2}\int_{-\infty}^{+\infty}\int_{-\infty}^{+\infty} F(x,y)e^{-\mathbf{i}(\alpha x+\beta y)}dxdy, \tag{13}$$

$$F(x,y) = \int_{-\infty}^{+\infty}\int_{-\infty}^{+\infty} \widetilde{F}(\alpha,\beta)\ e^{\mathbf{i}(\alpha x+\beta y)}d\alpha d\beta. \tag{14}$$

Performing the Fourier transform on each term shown in Eq. (12), the first component in the actual wavenumber vector $\underline{\alpha} = (\alpha,\beta)$ can be derived as

$$\alpha \simeq \frac{-\mathbf{i}}{h}(a_1e^{-\mathbf{i}(\alpha h+\beta h)} + a_2e^{-\mathbf{i}\beta h} + a_3e^{\mathbf{i}(\alpha h-\beta h)} + a_4e^{-\mathbf{i}\alpha h} + a_5 + a_6e^{\mathbf{i}\alpha h} + a_7e^{-\mathbf{i}(\alpha h-\beta h)} + a_8e^{\mathbf{i}\beta h} + a_9e^{\mathbf{i}(\alpha h+\beta h)} + a_{10}e^{\mathbf{i}(-2\beta h)} + a_{11}e^{\mathbf{i}(2\beta h)} + a_{12}e^{\mathbf{i}(-2\alpha h)}), \tag{15}$$

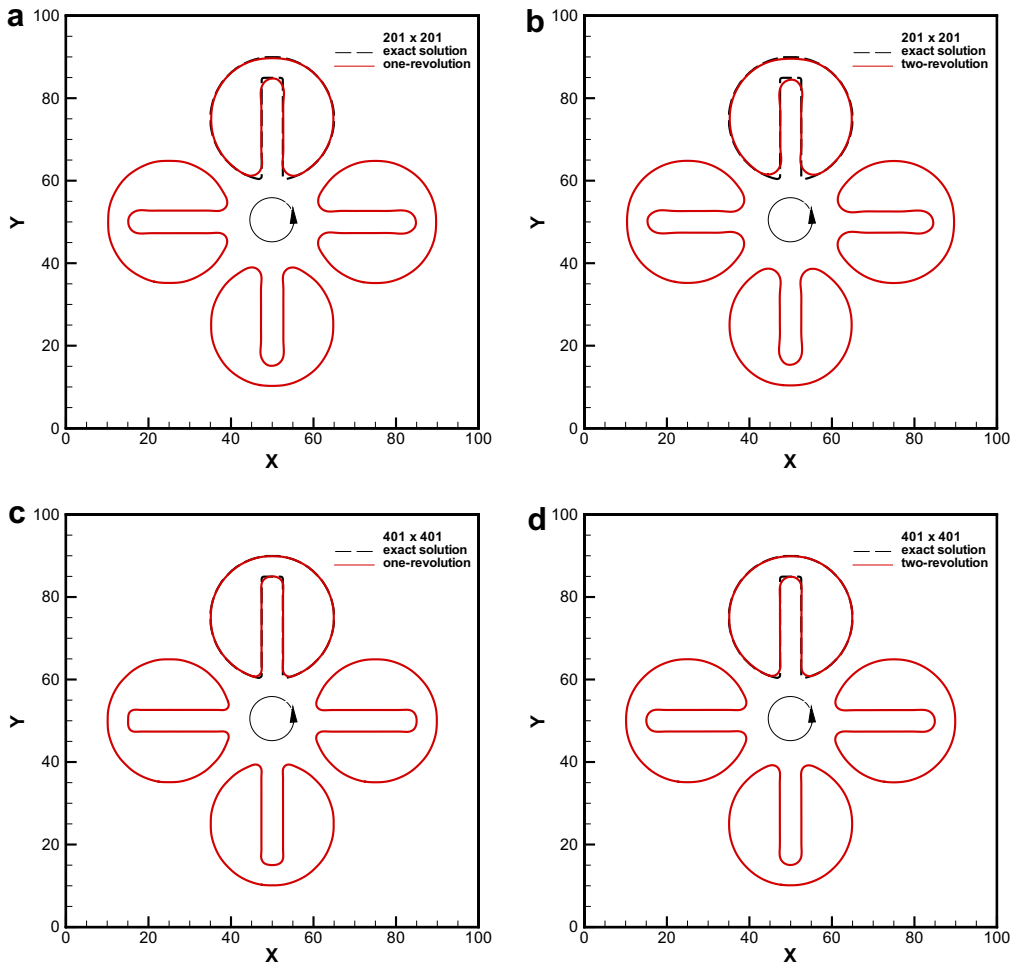

Fig. 6. The contours of $\Phi = 0.5$ predicted at two grids after one and two revolutions. (a) 201×201 grids; (b) 201×201 grids; (c) 401×401 grids; (d) 401×401 grids.

where $\mathbf{i} = \sqrt{-1}$. In an approximated sense, the components of the effective wavenumber vector $\underline{\tilde{\alpha}} = (\tilde{\alpha}, \tilde{\beta})$ can be written as follows:

$$\tilde{\alpha} = \frac{-\mathbf{i}}{h}(a_1 e^{-\mathbf{i}(\alpha h+\beta h)} + a_2 e^{-\mathbf{i}\beta h} + a_3 e^{\mathbf{i}(\alpha h-\beta h)} + a_4 e^{-\mathbf{i}\alpha h} + a_5 + a_6 e^{\mathbf{i}\alpha h} + a_7 e^{-\mathbf{i}(\alpha h-\beta h)} + a_8 e^{\mathbf{i}\beta h} + a_9 e^{\mathbf{i}(\alpha h+\beta h)} + a_{10} e^{\mathbf{i}(-2\beta h)} + a_{11} e^{\mathbf{i}(2\beta h)} + a_{12} e^{\mathbf{i}(-2\alpha h)}), \tag{16}$$

$$\tilde{\beta} = \frac{-\mathbf{i}}{h}(b_1 e^{-\mathbf{i}(\alpha h+\beta h)} + b_2 e^{-\mathbf{i}\beta h} + b_3 e^{\mathbf{i}(\alpha h-\beta h)} + b_4 e^{-\mathbf{i}\alpha h} + b_5 + b_6\, e^{\mathbf{i}\alpha h} + b_7 e^{-\mathbf{i}(\alpha h-\beta h)} + b_8 e^{\mathbf{i}\beta h} + b_9 e^{\mathbf{i}(\alpha h+\beta h)} + b_{10} e^{\mathbf{i}(-2\beta h)} + b_{11} e^{\mathbf{i}(2\beta h)} + b_{12} e^{\mathbf{i}(-2\alpha h)}). \tag{17}$$

In this study, the magnitude of $|\alpha h - \tilde{\alpha} h|^2$ or the following integrated error E was assigned to be equal to zero in the following weak sense to make $\tilde{\alpha}$ to be an appropriate approximation of α [23–25]:

$$E(\alpha) = \int_{-\frac{\pi}{2}}^{\frac{\pi}{2}} \int_{-\frac{\pi}{2}}^{\frac{\pi}{2}} |\alpha h - \tilde{\alpha} h|^2 d\gamma_1 d\gamma_2. \tag{18}$$

Note that $(\gamma_1, \gamma_2)(\equiv (\alpha h, \beta h))$, where $-\frac{\pi}{2} \leqslant \gamma_1, \gamma_2 \leqslant \frac{\pi}{2}$, should sufficiently define a period of sine (or cosine) wave.

To minimize the value of E, it is required to enforce $\frac{\partial E}{\partial a_6} = 0$ at the stencil point $(i+1, j)$. Therefore, the values for $a_1 = a_3 = a_7 = a_9 = \frac{1}{18}\frac{\pi(3\pi-10)}{(\pi^2-6\pi+8)}$, $a_2 = a_8 = \frac{1}{9}\frac{\pi(3\pi-10)}{(3\pi-8)}$, $a_4 = \frac{-4}{9}\frac{(3\pi^2-16\pi+18)}{(\pi^2-6\pi+8)}$, $a_6 = -\frac{8}{9}\frac{(\pi-3)}{9(\pi^2-6\pi+8)}$, $a_5 = \frac{1}{18}\frac{(21\pi^2-94\pi+72)}{(\pi^2-6\pi+8)}$, $a_{10} = a_{11} = 0$ and $a_{12} = \frac{1}{6}$ can be obtained. The resulting modified equation for F_x approximated by means of Eq. (12) is shown to have a spatial accuracy order of third in the sense of $F_x \simeq 0.08333h^3 F_{xxxx} - 0.03333h^4 F_{xxxxx} + 0.00854h^5 F_{xxxxyy} +$

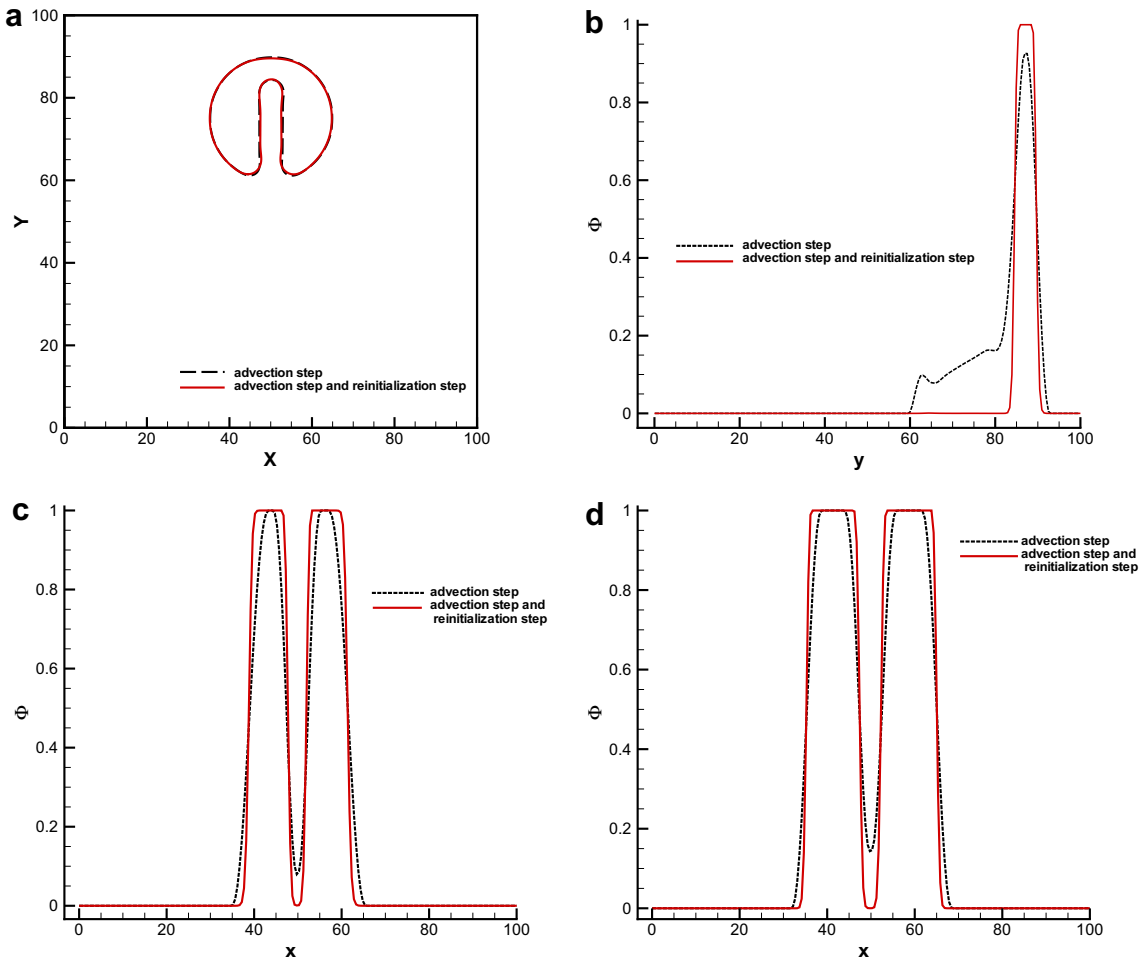

Fig. 7. The predicted solutions for Φ after two revolutions in a mesh with 201×201 nodal points using the advection step equation (or Eq. (8)), advection step and reinitialization step equations (or Eqs. (8) and (11)). (a) contours of $\Phi = 0.5$; (b) $\Phi(50, y)$; (c) $\Phi(x, 65)$; (d) $\Phi(x, 75)$.

$0.01388h^5F_{xxxxxx} + 0.008537427877049h^5F_{xxyyyy} + \cdots + \text{H.O.T.}$ Similarly, the 12-point stencil discrete equation for F_y, which accommodates the dispersion relation property, in the case of $v > 0$ can be derived by the same way as that of F_x.

5. Incompressible flow solver in non-staggered grids

Regularized methods developed for solving the computationally difficult Navier–Stokes equations along with the incompressibility constraint condition are rooted in replacing the divergence-free constraint equation for mass conservation with a differential equation for pressure or pressure variation. The fractional step and artificial compressibility methods are the two representative classes. In the artificial compressibility method, the constraint equation for the velocity field, or the momentum equation, can be regularized by adding a pseudo-time dependent term $\frac{1}{\beta_a}\frac{\partial p}{\partial \tau}$ to the left hand side of the continuity equation. The equation for mass conservation turns out to be the equation for p as $\frac{1}{\beta_a}\frac{\partial p}{\partial \tau} + \nabla \cdot \underline{u} = 0$, where β_a is the user's specified artificial compressibility coefficient ($\beta_a = 10 \sim 500$ was normally recommended).

In fractional-step methods, calculation of the solutions can be generally decomposed into two or three steps. The first step approximates the viscous and convective terms to obtain an intermediate velocity from the transport equation for $\underline{u}$, with the pressure term being omitted. To make the fractional-step method viable for solving the incompressible equations, the time increment should be split based on the Helmholtz–Hodge decomposition theorem [26]. Any vector field $\underline{w}$ can be decomposed into a solenoidal field with a zero normal component along the boundary and a gradient of some scalar functions. By choosing the scalar function as the pressure p and the divergence-free vector field as the velocity $\underline{u}$, the equation given by $\underline{u} = \underline{w} - \nabla p$ is resulted from the underlying decomposition theorem. The operator P is defined to project the vector $\underline{w}$ ($\equiv \underline{u} + \nabla p$) onto its divergence-free vector field $\underline{u}$, thereby rendering $P\underline{w}$ as $P\underline{u} + P(\nabla p)$. According to this definition, we can derive $P\underline{w} = P\underline{u} = \underline{u}$ and, in turn, $P(\nabla p) = 0$. This projection operator is then applied to both hand sides of the momentum equation. Since $\underline{u}$ is divergence-free, we can get $P\left(\frac{\partial \underline{u}}{\partial t}\right) = \frac{\partial \underline{u}}{\partial t}$ and can, therefore, derive

$$\frac{\partial \underline{u}}{\partial t} = P\left(-(\underline{u}\cdot\nabla)\underline{u} - \frac{\nabla p}{\rho} + \frac{1}{\rho Re}\nabla\cdot(2\mu\mathbf{D}) + \underline{f}\right) \tag{19}$$

where $\underline{f}$ is expressed as $-\frac{1}{\rho}\frac{1}{We}\kappa(\Phi)\nabla\Phi + \frac{1}{Fr^2}\underline{e}_g$.

Thanks to the above theoretical splitting, the vector field can be decomposed into the zero-curl and zero-divergence two components. The intermediate velocity $\underline{u}^{n+\frac{1}{2}}$ can then be calculated from the fully implicit equation along with the prescribed velocity $\underline{u}^{n+\frac{1}{2}}|_{\partial\Omega}(\equiv \underline{b})$ along the boundary $\partial\Omega$ as follows for the conventional Navier–Stokes vector equation

$$\frac{\underline{u}^{n+\frac{1}{2}} - \underline{u}^n}{\Delta t} = -(\underline{u}^{n+\frac{1}{2}}\cdot\nabla)\underline{u}^{n+\frac{1}{2}} + \frac{1}{\rho Re}\nabla\cdot(2\mu\mathbf{D}^{n+\frac{1}{2}}) + \underline{f}^{n+1}. \tag{20}$$

It is worthy to note that the pressure variable has been eliminated from the momentum equations so that analysis of the incompressible viscous equations becomes much simplified. The above equation can be solved sequentially from the advection step, given by $\frac{\underline{u}_a^{n+\frac{1}{2}} - \underline{u}^n}{\Delta t} + (\underline{u}^n\cdot\nabla)\underline{u}^n = 0$, and the diffusion step, given by $\frac{\underline{u}^{n+\frac{1}{2}} - \underline{u}_a^{n+\frac{1}{2}}}{\Delta t} = \frac{1}{\rho Re}\nabla\cdot(2\mu\mathbf{D}^{n+\frac{1}{2}}) + \underline{f}^{n+\frac{1}{2}}$. Since the intermediate velocity solution $\underline{u}^{n+\frac{1}{2}}$ obtained from the above two steps does not necessarily satisfy the divergence-free constraint condition, the intermediate field $\underline{u}^{n+\frac{1}{2}}$ (or $\underline{w}$ given in $\underline{u} = \underline{w} - \nabla p$) can be decomposed into the sum of the solenoidal velocity $\underline{u}^{n+1}$ and the gradient of the currently chosen scalar function, which is proportional to $\Delta t\nabla p^{n+1}$. The integrity of employing the following two equations in the projection step is enlightened

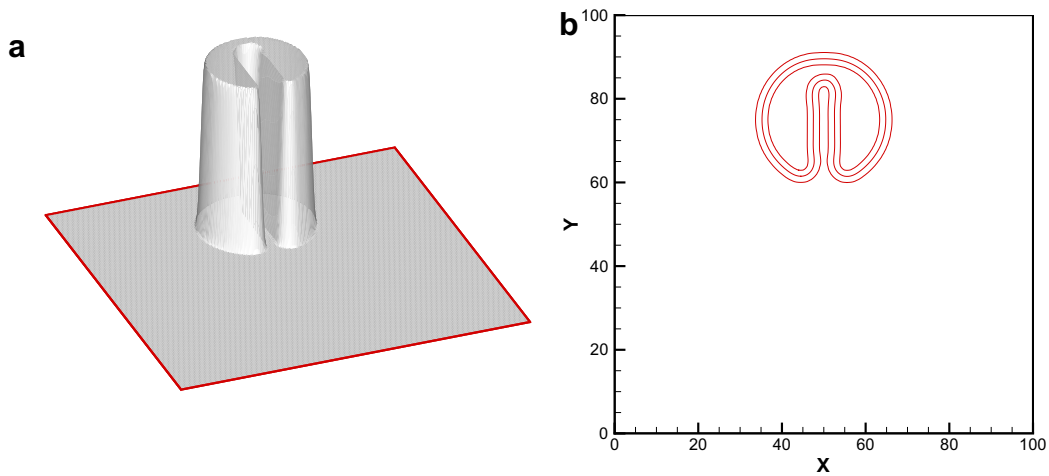

Fig. 8. The conservative level set solutions obtained at 201×201 grids after two revolutions by solving advection step and reinitialization step. (a) three-dimensional view of the predicted solution; (b) the predicted contours for $\Phi = 0.05$ (outer), 0.5 (middle) and 0.95 (inner).

$$\frac{\underline{u}^{n+1}-\underline{u}^{n+\frac{1}{2}}}{\Delta t}=\frac{\nabla p^{n+1}}{\rho}, \tag{21}$$

$$\nabla\cdot\underline{u}^{n+1}=0. \tag{22}$$

According to Eq. (21), calculation of $\underline{u}^{n+1}$ needs a pressure solution. By applying the divergence operator to both hand sides of $\underline{u}=\underline{w}-\nabla p$, the Poisson equation given by $\nabla\cdot\frac{\nabla p}{\rho}=\nabla\cdot\underline{u}^{n+\frac{1}{2}}$ can be derived. Controversy regarding the necessity of specifying the pressure boundary value in this formulation is arisen since no pressure boundary value needs to be specified when solving the primitive-variable Navier–Stokes equations. In addition, analysis of the Poisson equation for p is normally expensive. For these two reasons, in the following the regularization method is proposed.

Development of the regularization method for $\frac{\partial\underline{u}}{\partial\underline{t}}+(\underline{u}\cdot\nabla)\underline{u}=-\frac{\nabla p}{\rho}+\frac{1}{Re}\nabla^2\underline{u}+\underline{f}$ begins with the substitution of $\frac{\underline{u}^{n+1}-\underline{u}^{n+\frac{1}{2}}}{\Delta t}=\frac{\nabla p^{n+1}}{\rho}$ (or Eq. (21)) into the semi-discretized momentum equation given below

$$\frac{\underline{u}^{n+1}-\underline{u}^{n}}{\Delta t}+(\underline{u}^{n+1}\cdot\nabla)\underline{u}^{n+1}-\frac{1}{\rho Re}\nabla^2\underline{u}^{n+1}+\frac{\nabla p^{n+1}}{\rho}+\underline{f}^{n+1}=0. \tag{23}$$

This substitution yields

$$\frac{\underline{u}^{n+1}-\underline{u}^{n}}{\Delta t}+(\underline{u}^{n+\frac{1}{2}}\cdot\nabla)\underline{u}^{n+\frac{1}{2}}-\frac{1}{\rho Re}\nabla^2\underline{u}^{n+\frac{1}{2}}+\frac{\nabla p^{n+1}}{\rho}=M_1+M_2-\underline{f}^{n+1}, \tag{24}$$

where $M_1=[(\underline{u}^{n+\frac{1}{2}}\cdot\nabla)\nabla p^{n+1}+(\nabla p^{n+1}\cdot\nabla)\underline{u}^{n+\frac{1}{2}}-\frac{1}{Re}\nabla^2(\nabla p^{n+1})]\Delta t$ and $M_2=-[(\nabla p^{n+1}\cdot\nabla)\nabla p^{n+1}]\Delta t^2$. Let $p^{n+1}=p^*+p\prime$, where p^* is initially chosen to be the convergent solution p^n. Afterwards, the value of p^* will be chosen as the most updated pressure solution. The pressure-gradient step is decomposed into the following two steps

$$\frac{\underline{u}^{*}-\underline{u}^{n+\frac{1}{2}}}{\Delta t}=-\frac{\nabla p^{*}}{\rho}, \tag{25}$$

$$\frac{\underline{u}^{n+1}-\underline{u}^{*}}{\Delta t}=-\frac{\nabla p'}{\rho}. \tag{26}$$

Then, Eq. (24) can be reformulated as

$$\frac{\underline{u}^{n+1}-\underline{u}^{n}}{\Delta t}+(\underline{u}^{*}\cdot\nabla)\underline{u}^{*}-\frac{1}{\rho Re}\nabla^2\underline{u}^{*}+\frac{\nabla p^{*}}{\rho}=-\frac{\nabla p}{\rho}\prime+M_3+M_4-\underline{f}^{n+1}, \tag{27}$$

where

$$M_3=\left[(\underline{u}^{*}\cdot\nabla)\frac{\nabla p'}{\rho}+\left(\frac{\nabla p'}{\rho}\cdot\nabla\right)\underline{u}^{*}-\frac{1}{\rho Re}\nabla^2\left(\frac{\nabla p'}{\rho}\right)\right]\Delta t, \tag{28}$$

$$M_4=-\left[\left(\frac{\nabla p'}{\rho}\cdot\nabla\right)\frac{\nabla p'}{\rho}\right]\Delta t^2. \tag{29}$$

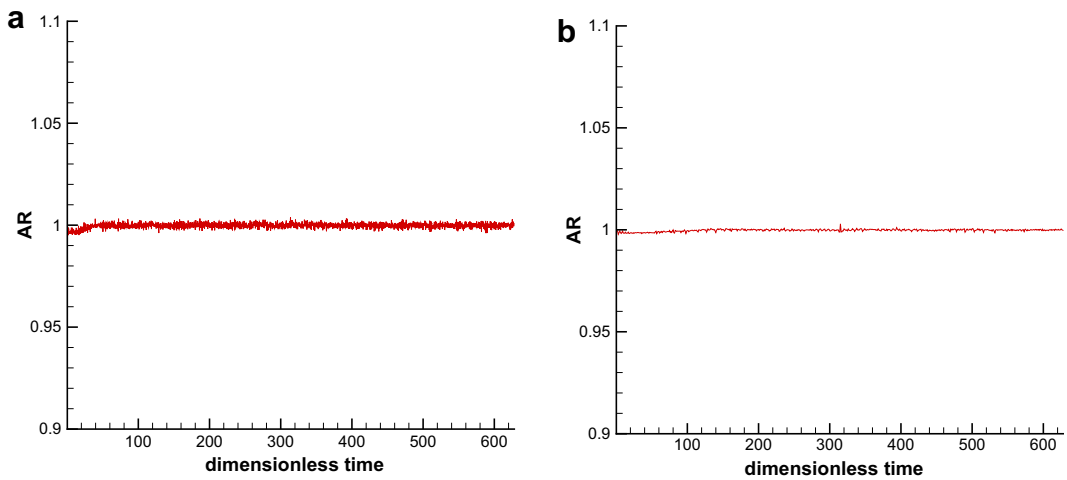

Fig. 9. The predicted area ratios (AR) against time for the cases carried out in two grids. (a) 201 × 201 grids; (b) 401 × 401 grids. Note that AR is defined as $\mathrm{AR}=\frac{\int\Phi(x,y;\ \text{for}\ 0.5\leqslant\Phi\leqslant1,t)dA}{\int\Phi(x,y;\ \text{for}\ 0.5\leqslant\Phi\leqslant1,t=0)dA}$.

By taking the divergence of Eq. (26) and imposing the constraint condition given by $\nabla \cdot \underline{u}^{n+1} = 0$, Eq. (28) can be rewritten as

$$M_3 = \left[(\underline{u}^* \cdot \nabla)\frac{\nabla p'}{\rho} + \left(\frac{\nabla p'}{\rho} \cdot \nabla\right)\underline{u}^* \right]\Delta t - \frac{1}{\rho Re}\nabla(\nabla \cdot \underline{u}^*). \tag{30}$$

As Eq. (27) indicates, the introduced momentum source term $M_{DFC}(\equiv -\Delta p' + M_3 + M_4)$ replaces the divergence-free condition and it can be called as the divergence-free-condition (DFC) compensated momentum source term. In other words, the idea of the proposed compensated method is to replace the divergence-free constraint condition with the source term M_{DFC} added to the momentum equations. Note that the Lin's SRM method [27] falls also into the category of the DFC method provided that $M_{DFC} = \lambda\nabla(\nabla \cdot \underline{u}_s)$ and $p' = \lambda(\nabla \cdot \underline{u}_s)$ in the course of iteration, where the subscript s (=1, 2, ...) represents the iteration counter. As the divergence-free constraint condition is satisfied, the DFC momentum source will be vanished. For the steady state analysis, the tolerance defined by $E((\equiv \max|\mathbb{E}^{k+1} - \mathbb{E}^k|))$, where $\mathbb{E}$ represents the field variable for $\underline{u}$ or p, is set as $E \leqslant 10^{-6}$. For the transient case, the time-accurate solution will be iteratively calculated. After obtaining the updated values of $\underline{u}^{n+1}$ and p^* at every iteration, they will be substituted into the left-hand side of Eq. (24) to calculate the momentum source term. As the momentum source term becomes less than 10^{-4}, the predicted solution at each time step can be assumed to be convergent. Normally, less than fifteen iterations will be needed to reach the convergent solutions.

Now, the remaining issue of developing the compensated method is to derive the equation for p'. By performing the divergence operator on Eq. (26), we get

$$\nabla \cdot \underline{u}^{n+1} = \nabla \cdot \underline{u}^* - \Delta t \nabla \cdot \frac{\nabla p'}{\rho}. \tag{31}$$

Enforcement of the divergence-free condition $\nabla \cdot \underline{u}^{n+1} = 0$ leads to

$$\nabla \cdot \frac{\nabla p'}{\rho} = \frac{\nabla \cdot \underline{u}^*}{\Delta t}. \tag{32}$$

At each interior point (i,j), application of a central approximation for the left-hand side of Eq. (32) leads to

$$\left(\frac{1}{\rho_{i+\frac{1}{2}}\Delta x^2} + \frac{1}{\rho_{i-\frac{1}{2}}\Delta x^2} + \frac{1}{\rho_{j+\frac{1}{2}}\Delta y^2} + \frac{1}{\rho_{j-\frac{1}{2}}\Delta y^2}\right)p'_{i,j} = -\frac{\nabla \cdot \underline{u}^*_{i,j}}{\Delta t} + \frac{p'_{i-1,j}}{\rho_{i-\frac{1}{2}}\Delta x^2} + \frac{p'_{i+1,j}}{\rho_{i+\frac{1}{2}}\Delta x^2} + \frac{p'_{i,j-1}}{\rho_{j-\frac{1}{2}}\Delta x^2} + \frac{p'_{i,j-1}}{\rho_{j-\frac{1}{2}}\Delta x^2}. \tag{33}$$

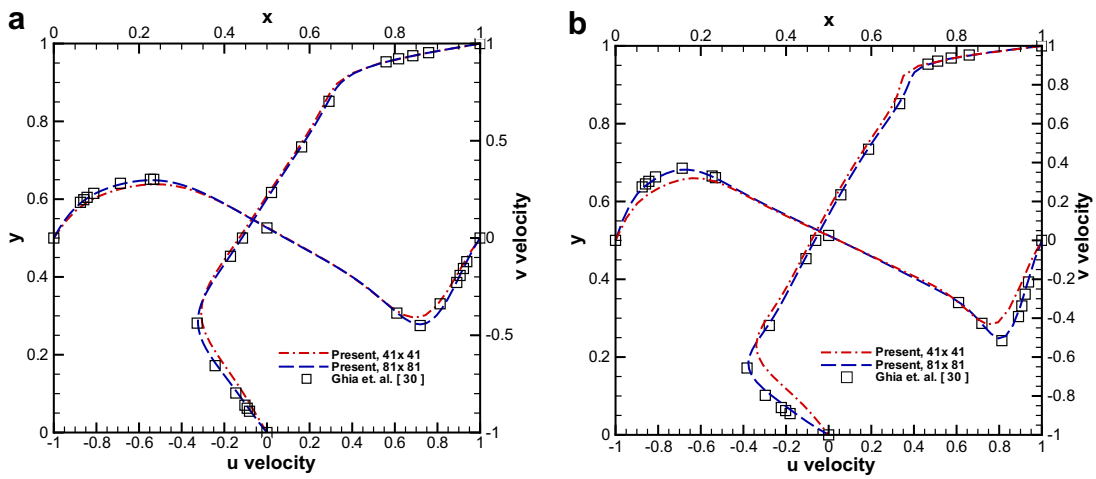

Fig. 10. Comparison of the predicted mid-plane velocity profiles for the cases investigated at two Reynolds numbers. (a) $Re = 400$; (b) $Re = 1000$.

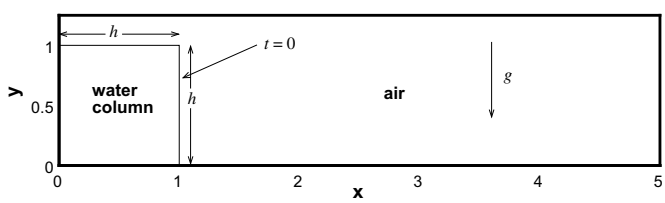

Fig. 11. Schematic of the initial water column for the dam break problem considered in Section 7.1. The diffusion coefficient is prescribed by $\bar{\mu} = \Delta x$.

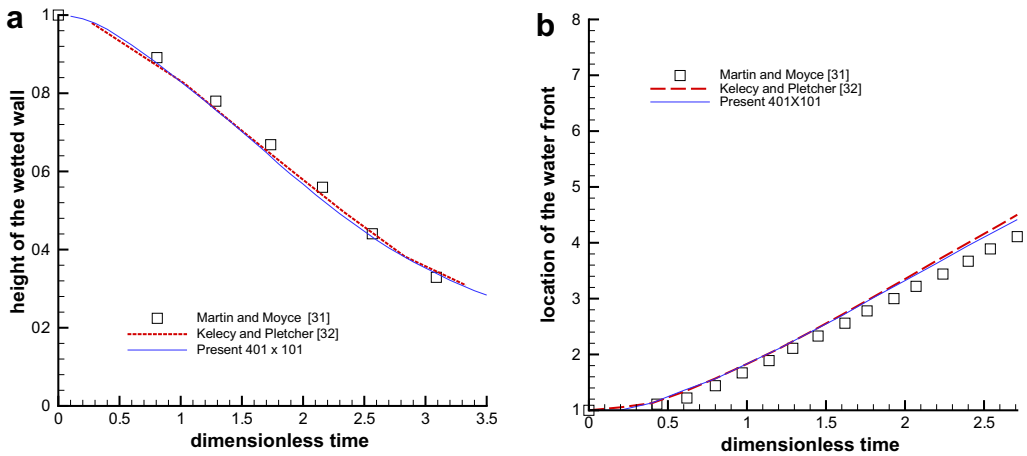

Fig. 12. Comparison of the predicted surge front location and the water column height with the experimental data and the numerical results of Kelecy and Pletcher. (a) height of the wetted wall; (b) location of the water front.

By omitting $\frac{(p'_{i-1,j})}{\rho_{i-\frac{1}{2}}\Delta x^2} + \frac{(p'_{i+1,j})}{\rho_{i+\frac{1}{2}}\Delta x^2} + \frac{(p'_{i,j-1})}{\rho_{j-\frac{1}{2}}\Delta x^2} + \frac{(p'_{i,j-1})}{\rho_{j-\frac{1}{2}}\Delta x^2}$, the following equation can be derived:

$$p'_{i,j} = -\frac{\nabla \cdot \underline{u}^*_{i,j}}{\Delta t\left(\frac{1}{\rho_{i+\frac{1}{2}}\Delta x^2} + \frac{1}{\rho_{i-\frac{1}{2}}\Delta x^2} + \frac{1}{\rho_{j+\frac{1}{2}}\Delta y^2} + \frac{1}{\rho_{j-\frac{1}{2}}\Delta y^2}\right)}. \tag{34}$$

Since the above omission may over-predict the solution p', compensation for the omitted two terms will be made as follows. First, Eq. (34) is used to calculate the predicted pressure correction $p^{*\prime}$ given by

$$p'^*_{i,j} = -\frac{\nabla \cdot \underline{u}^*_{i,j}}{\Delta t\left(\frac{1}{\rho_{i+\frac{1}{2}}\Delta x^2} + \frac{1}{\rho_{i-\frac{1}{2}}\Delta x^2} + \frac{1}{\rho_{j+\frac{1}{2}}\Delta y^2} + \frac{1}{\rho_{j-\frac{1}{2}}\Delta y^2}\right)}. \tag{35}$$

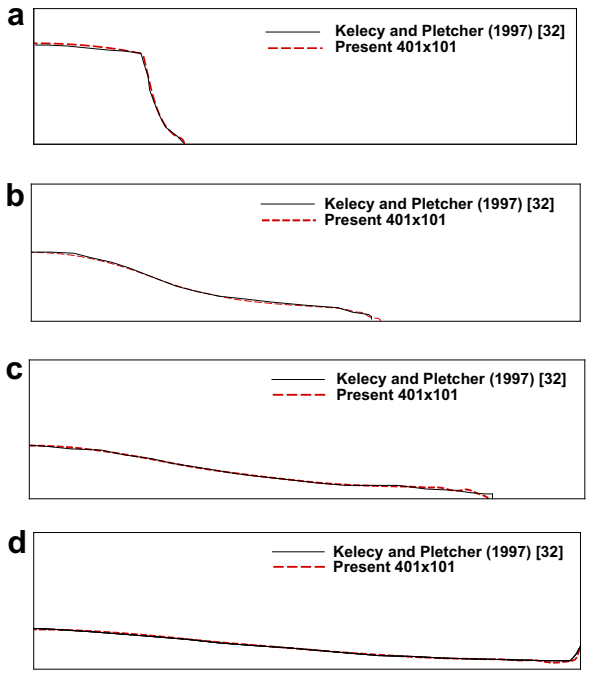

Fig. 13. Comparison of the predicted free surfaces, obtained at 401×101 grids, with those of Kelecy and Pletcher for the two-dimensional broken dam problem. (a) $t = 0.6$; (b) $t = 1.8$; (c) $t = 2.4$; (d) $t = 3.0$.

This is followed by calculating the pressure correction $p*$ from $p^{*\prime}$ by taking into account the omitted terms, which are evaluated from the $p^{*\prime}$ solutions. The resulting $p\prime$ solution at (i,j), for example, will be calculated according to

$$p'_{i,j} = p^{*\prime}_{i,j} + \frac{1}{\left(\frac{1}{\rho_{i+\frac{1}{2}}\Delta x^2} + \frac{1}{\rho_{i-\frac{1}{2}}\Delta x^2} + \frac{1}{\rho_{j+\frac{1}{2}}\Delta y^2} + \frac{1}{\rho_{j-\frac{1}{2}}\Delta y^2}\right)} \left(\frac{p^{*\prime}_{i-1,j}}{\rho_{i-\frac{1}{2}}\Delta x^2} + \frac{p^{*\prime}_{i+1,j}}{\rho_{i+\frac{1}{2}}\Delta x^2} + \frac{p^{*\prime}_{i,j-1}}{\rho_{j-\frac{1}{2}}\Delta x^2} + \frac{p^{*\prime}_{i,j-1}}{\rho_{j-\frac{1}{2}}\Delta x^2}\right). \tag{36}$$

It should be stressed that the under-relaxation procedure becomes no longer needed. In summary, given the divergence-free initial velocity vector, the velocity vector $\underline{u}$ at the time step $(n+1)$ can be computed explicitly from Eq. (27). Two invoked source terms M_3 and M_4 can be computed respectively from Eqs. (29) and (30). As for the source term $-\nabla p'$, it is approximated by the central scheme $\left(\text{or} p'_{i,j} = \frac{p'_{i+1,j} - p'_{i-1,j}}{2\Delta x}\right)$ using the p' values computed from Eqs. (35) and (36). The pressure solution $p_{i,j}$ at $(n+1)\Delta t$ is then computed by $p^{n+1}_{i,j} = p^*_{i,j} + p'_{i,j}$, where p^* is the known convergent solution calculated at the previous time (or $p^n_{i,j}$).

While the even–odd pressure oscillations can be well eliminated in staggered grids, the resulting programming complexity motivated us to discretize ∇p in non-staggered meshes, where the velocities and pressure are stored at the same point. To avoid spurious pressure oscillations, the nodal value of $p_{i,j}$ should be taken into account while approximating ∇p at the nodal

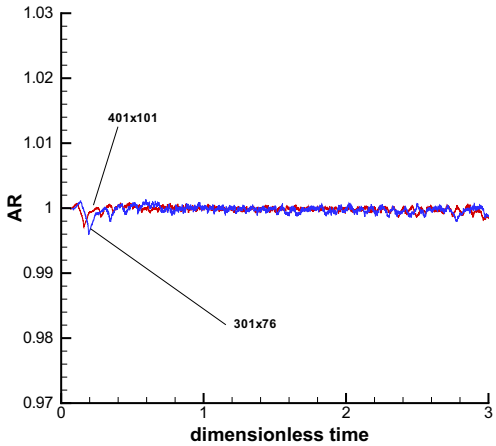

Fig. 14. The predicted area ratios (AR) against the dimensionless time for the cases carried out in grids with 301 × 76 and 401 × 101 resolutions. Note that AR is defined as $\text{AR} = \frac{\int \Phi(x,y;\ \text{for}\ 0.5 \leqslant \Phi \leqslant 1, t) dA}{\int \Phi(x,y;\ \text{for}\ 0.5 \leqslant \Phi \leqslant 1, t=0) dA}$.

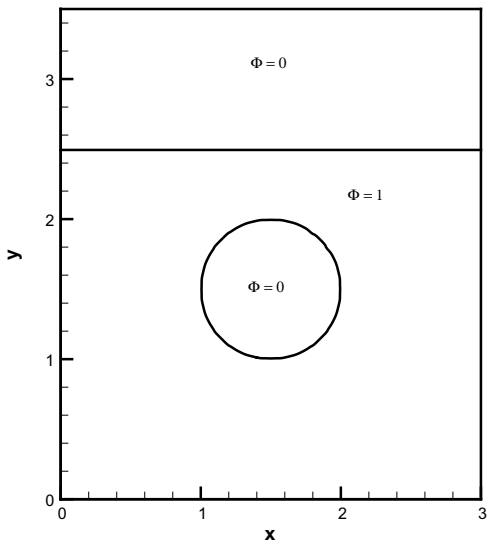

Fig. 15. Schematic of the initial condition for the bubble rising problem given in Section 7.2.

point (i,j). In this study the approximated value of p_x (or $G_{i,j}$ $(\equiv h\ p_x|_{i,j})$, where h denotes the constant mesh size, at an interior node (i,j) will be computed from the following compact implicit equation

$$c_1 G_{i+1,j} + c_2 G_{i,j} + c_3 G_{i-1,j} = c_4(p_{i+2,j} - p_{i+1,j}) + c_5(p_{i+1,j} - p_{i,j}) + c_6(p_{i,j} - p_{i-1,j}) + c_7(p_{i-1,j} - p_{i-2,j}). \tag{37}$$

The readers can refer to [28] for a detailed derivation of $c_1 \sim c_7$ by expanding $G_{i\pm1,j}$ in Taylor series with respect to $G_{i,j}$ and $p_{i\pm1,j}$ and $p_{i\pm2,j}$ with respect to $p_{i,j}$.

6. Verification studies

Three classical problems will be chosen to verify the proposed dispersion-relation-preserving advection scheme and the incompressible Navier–Stokes equations, respectively.

6.1. Rotation of Vortex

We investigated the problem of Olsson and Kreiss [12] in a square domain with the specified velocity field given by $u = \sin^2(\pi x)\sin(2\pi y)$, $v = -\sin^2(\pi y)\sin(2\pi x)$. The center of this rotating velocity field, defined in a circle of radius 0.15, is

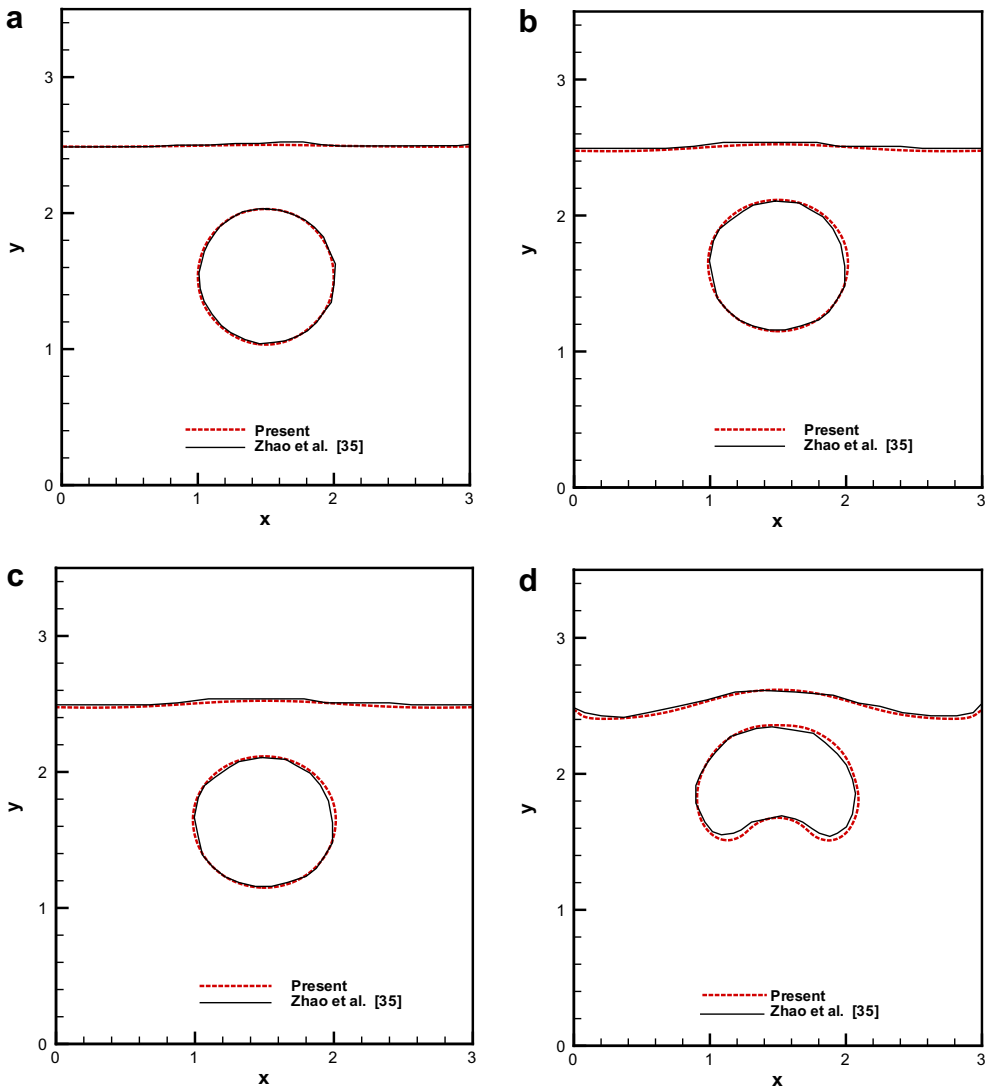

Fig. 16. Comparison of the predicted time–evolving free surfaces and bubble interfaces, obtained at 241×281 grids, with those of [35] for the case without considering surface tension. The diffusion coefficient is prescribed by $\bar{\mu} = \Delta x$. (a) $t = 0.5$; (b) $t = 1.0$; (c) $t = 1.5$; (d) $t = 2.0$ (e) $t = 2.5$; (f) $t = 3.0$; (g) $t = 3.5$; (h) $t = 4.0$.

$(0.5, 0.75)$. At $t = T(= 1.0)$, the flow field was made to be reversed so that the exact solution at $t = 2T$ should theoretically coincide with the initial condition. The test problem will be solved on 257×257 grids and at $\Delta t = \frac{1}{10,000}$. For the case with $\bar{\mu} = \Delta x$, shown in Eq. (11), the predicted results at $t = 0, 0.5, 1.0$ and 2.0 are plotted in Fig. 1. Calculation is followed by performing a non-reversion simulation in the 257×257 grid system until $t = 2$. The solutions at $t = 1$ and $t = 2$ are shown in Fig. 2(a) and (b). For the sake of comparison, the results in [12] are plotted in Fig. 2(c) and (d). To further confirm that our prediction is accurate, we plot the predicted values of AR against time in Fig. 3, from which the area is seen to be conserved fairly well.

For the sake of completeness, we also calculate the spatial rate of convergence by performing calculations on five grids $(61)^2, (101)^2, (141)^2, (181)^2, (221)^2$. The time step is chosen to be $\Delta t = \frac{1}{10,000}$. Since $\Delta t \ll min\{\Delta x\}$, the predicted errors come mainly from the approximation of the spatial derivative terms. At $t = 1.0$, the predicted error norms and the corresponding spatial rates of convergence for the problem with velocity being reversed at $t = T(= 0.5)$ are tabulated in Table 1. The convergence rates will be determined by the predicted L_1-error norms, defined by $\int_\Omega |H(\Phi_{\text{numerical}}) - H(\Phi_{\text{exact}})|/L d\Omega$, where $H(\Phi) = \begin{cases} 0 & \text{if } \Phi < 0.5 \\ 1 & \text{if } \Phi > 0.5 \end{cases}$ and L is the perimeter length. Based on the calculation we are led to know that the accuracy is decreased quite stably with the grid reduction with the convergent rate less than three (which is the order of the proposed DRP scheme). The deteriorated accuracy order is mainly due to the second-order approximation applied for calculating the normal vector term and the second-order approximation of the terms shown in the reinitialization step equation.

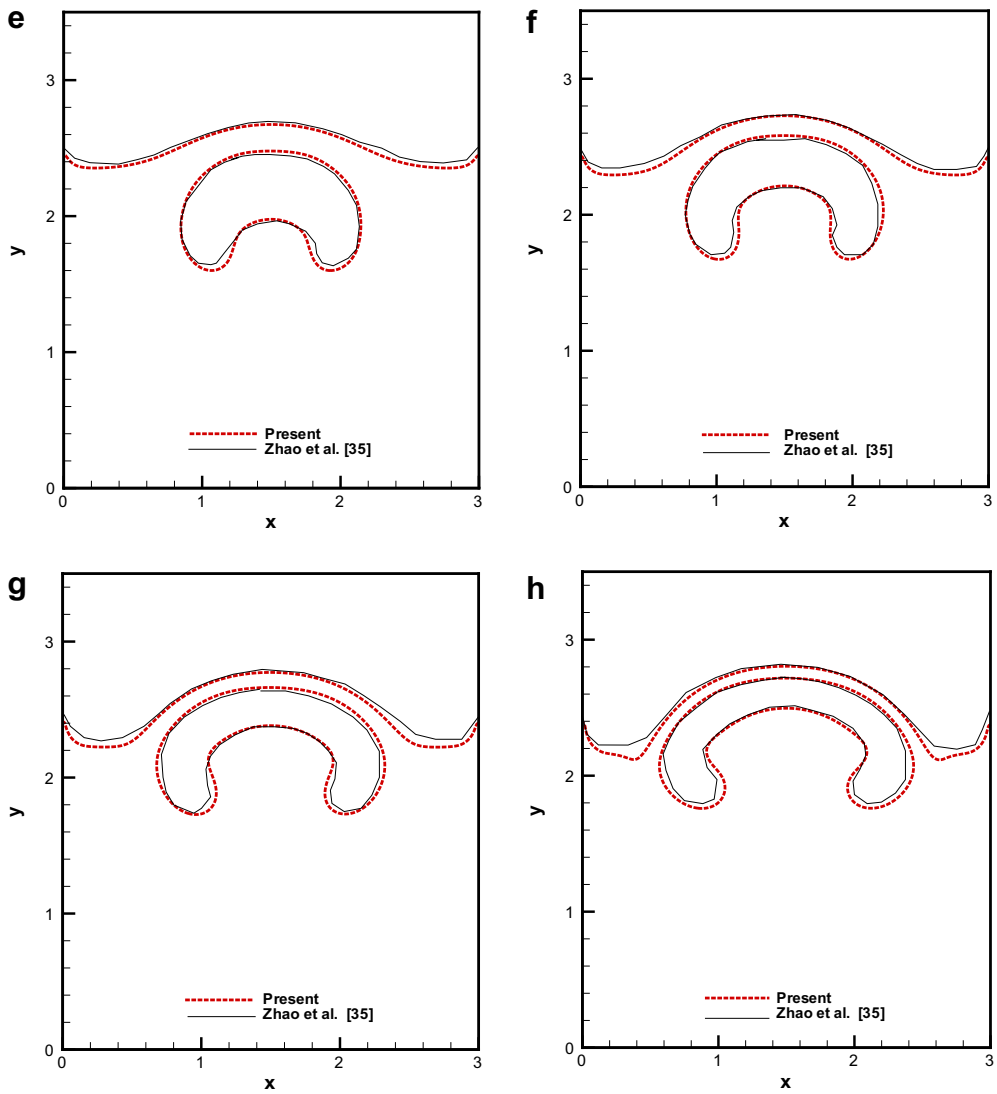

Fig. 16 (*continued*)

6.2. Rotation of a sharp slot profile

To verify the proposed DRP advection scheme, the problem of Zalesak [29] will be considered. The sharp profile of the notched disc with the slot width of 15, schematic in Fig. 4, is made to rotate about the point (50,75) in an inviscid flow with the velocity field given by $(u, v) = ((\pi/314)(50 - y), (\pi/314)(x - 50))$. This problem has been known to be a tough test for assessing the pure advection scheme for the solution with a large gradient. We carried out the calculation for the problem using 101×101 nodal points and compared the solution with the Pilliod and Puckett's result [29], which is shown in Fig. 5. We also carried out the calculation for the problem using 201×201 and 401×401 nodal points. After one and two revolutions, the solutions were compared and shown in Fig. 6. Good agreement with the exact solution schematic in the same figure is clearly seen. The dispersive error has been well eliminated for the case with 201×201 nodal points since the predicted solutions near the jump are seen to show only a negligibly small oscillation in Fig. 7. This implies that the solutions obtained from the DRP advection scheme for the approximation of advection terms involved in both solution steps of the conservative level set method are dispersively very accurate.

To enlighten that the employed nonlinear compressive flux term can indeed help to sharpen the discontinuous front, we plot in Fig. 7 the solution profile of Φ after the advection and reinitialization steps. Note that a small artificial viscosity,

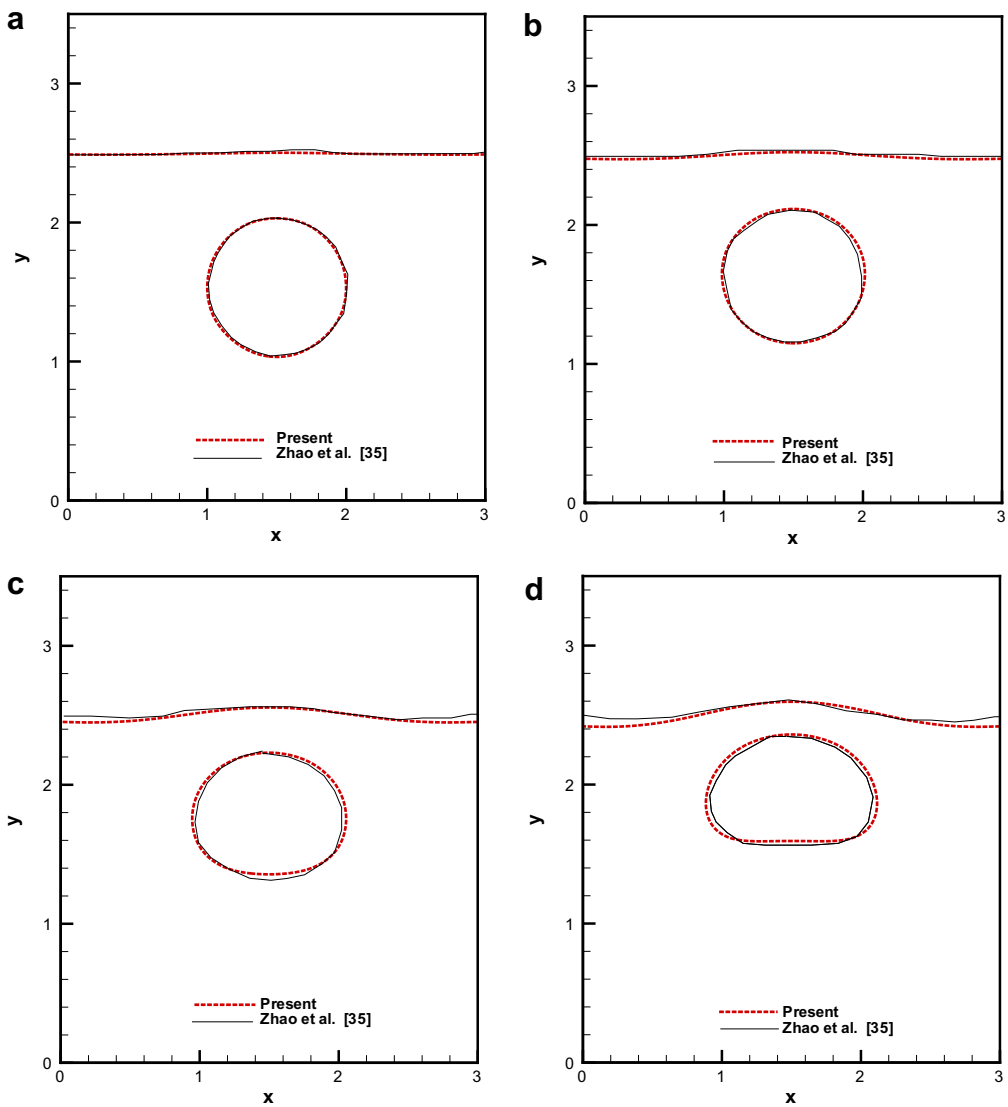

Fig. 17. Comparison of the predicted time–evolving free surfaces and bubble interfaces, obtained at 241×281 grids, with those of [35] for the case considering surface tension. The diffusion coefficient is prescribed by $\bar{\mu} = \Delta x$. (a) $t = 0.5$; (b) $t = 1.0$; (c) $t = 1.5$; (d) $t = 2.0$ (e) $t = 2.5$; (f) $t = 3.0$; (g) $t = 3.5$; (h) $t = 4.0$.

namely, $\bar{\mu} = \Delta x$ is introduced in the reinitialization step of the conservative level set method to smear the oscillations in the vicinity of the discontinuity. Also, the predicted solution contours shown in Fig. 8 for $\Phi = 0.05, 0.5, 0.95$ are seen to be irrelevant to the flow direction. In addition, the area ratios (AR) shown in Fig. 9 for the notched disk within the value range of $0 \leqslant \Phi \leqslant 1$ demonstrate the conservative property embedded in the transport equation for the level set function. It is, therefore, possible to capture the interface accurately and stably using the proposed two-dimensional DRP scheme.

6.3. Lid-driven cavity flow problem

The flow driven by a constant upper lid velocity $u_{\text{lid}}(= 1)$ in the square cavity is then investigated at $Re = 400$ and 1000. The simulated grid-independent mid-plane velocity profiles for $u(0.5, y)$ and $v(x, 0.5)$ are plotted in Fig. 10. Good agreement with the benchmark solutions of Ghia et al. [30] validates the proposed incompressible flow solver implemented in the two-dimensional non-staggered grids.

7. Numerical results

With the success in verifying the advection scheme and the incompressible flow solver, we are proceeded to justify the conservative level set method by virtue of the four investigated problems, which all involve the topological changes of inter-

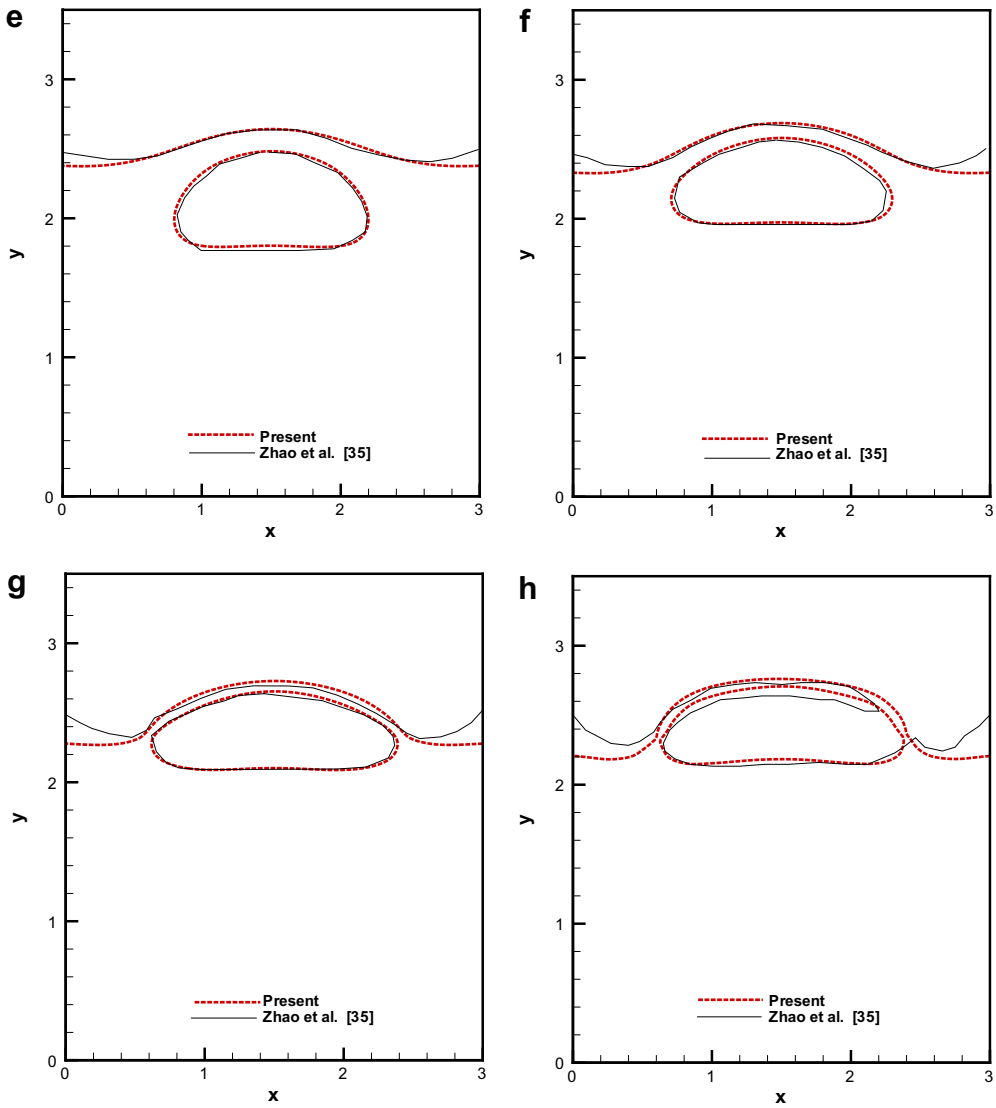

Fig. 17 (*continued*)

face. The first test problem, known as the dam break problem, is chosen to show the ability of the proposed interface capturing method for solving the problem without taking the surface tension into account. The second and third simulations are known as a rising air bubble in water and a droplet falling into water, respectively. Since the surface tension force present

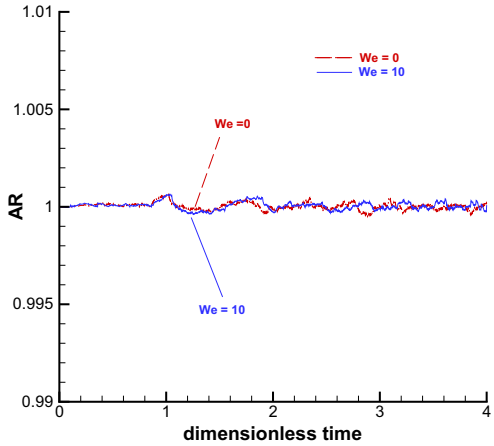

Fig. 18. Plots of the simulated area ratios (AR) against the dimensionless time for the rising bubble investigated at $We = 0$ and $We = 10$. Note that AR is defined as $\mathrm{AR} = \frac{\int \Phi(x,y;\ \text{for}\ 0.5 \leqslant \Phi \leqslant 1, t)dA}{\int \Phi(x,y;\ \text{for}\ 0.5 \leqslant \Phi \leqslant 1, t=0)dA}$.

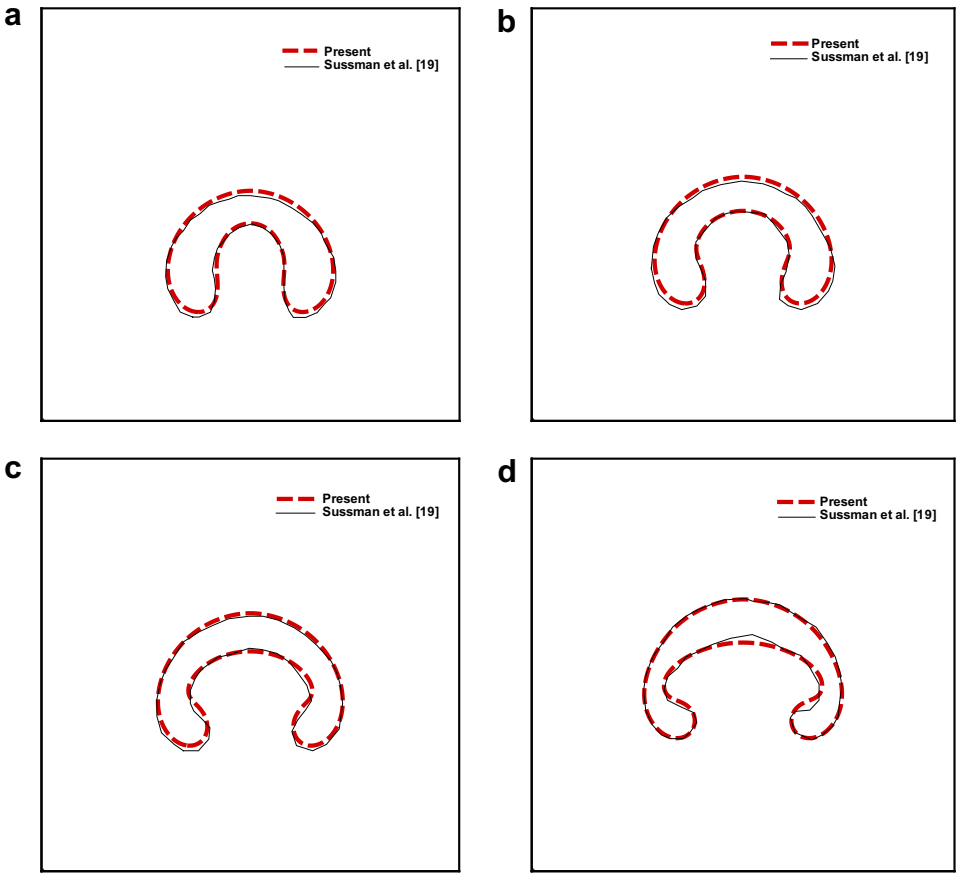

Fig. 19. Comparison of the predicted time-evolving free surfaces and bubble interfaces, obtained at 144×144 grids, with those of [19] for the case considering surface tension. The diffusion coefficient is prescribed by $\bar{\mu} = \Delta x$. (a) $t = 2.8$; (b) $t = 3.2$; (c) $t = 3.6$; (d) $t = 4.0$ (e) $t = 4.4$; (f) $t = 4.8$; (g) $t = 5.2$; (h) $t = 5.6$.

along the gas/water interface can play an ineligible role for the time–evolving air bubble or water droplet shapes, surface tension will be considered in both cases. Another well-known benchmark problem, known as the Rayleigh–Taylor problem, is also chosen for the validation sake.

7.1. Dam break problem

The first problem without considering surface tension simulates the sudden collapse of a rectangular column of water onto a planar surface. This classical problem, known as the dam break problem, has been frequently employed to validate the code for predicting free surface hydrodynamics. In addition to the hydraulic importance of this problem, both experimental [31] and numerical results [32] are available for making a direct comparison.

In the current calculation, the fluid properties are considered to be the same as those given in [32]. The initially prescribed height of the water column schematic in Fig. 11 is $h = 1$. The results for the collapsed water will be predicted at $Re = 42792$ in the domain containing 301×76 and 401×101 nodal points. The predicted heights of the collapsed water column will be plotted against the dimensionless time defined in [32]. Good agreement with the experimental result given in [31] is clearly demonstrated in Fig. 12 for the predicted surge front location and the water column height. The predicted time–evolving free surfaces in Fig. 13 are compared also favorably with the finite element solution of Kelecy and Pletcher [32]. As Fig. 14 shows for the ratio of the temporal water against the initial water column, the conservative property built in the modified level set method is still retained quite well.

7.2. Bubble rising problem in a partially filled container

We then investigate the time–evolving interface problem where surface tension needs to be taken into account. The problem under investigation considers the evolution of a stationary bubble, that is driven by surface tension, in a container partially filled with the viscous fluid of height $3.5D$ and width $3.0D$, where D is the initial diameter of the bubble. The main

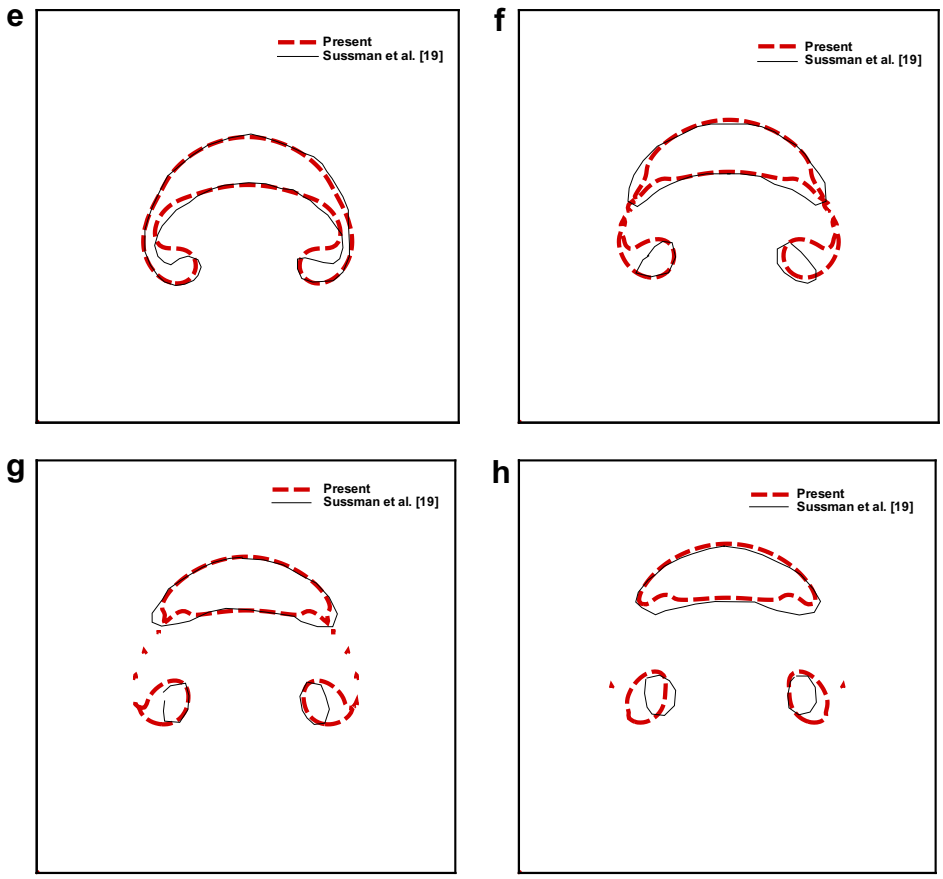

Fig. 19 (*continued*)

reason for modeling the gas bubble rising from rest in the incompressible fluid flow under buoyancy is due to a considerable amount of available experimental results in the literature [33,34].

Modelling of a rising bubble, schematic in Fig. 15, needs to specify the ratios of physical properties for the gas and liquid. The fluid–gas density and viscosity ratios are specified respectively as $\rho_l/\rho_g = 2.0$ and $\mu_l/\mu_g = 2.0$. In addition, the problem under investigation is characterized by another two dimensionless parameters, namely, $Re = (D)^{3/2}\sqrt{g}\rho_l/\mu_l$ and $We = \rho_l g D^2/\sigma$, where *Re* and *We* are denoted as the *Reynolds* and *Weber* numbers, respectively. The subscripts *l* and *g* correspond to the fluid surrounding the bubble and the fluid inside the bubble, respectively. Initially, the bubble center is located stationarily at $(1.5D, 1.5D)$ in the flow, which is at rest everywhere. The whole domain will be considered rather than simply specifying the axially symmetric condition to avoid a possible development of Conda effect. As is usual, no-slip conditions are specified along the horizontal and vertical walls.

Since surface tension can play an ineligible role during bubble rising, both cases with/without consideration of surface tension will be investigated at $Re = 200$. For the case taking into account the surface tension, the Weber number under current investigation will be set as $We = 10$. In Figs. 16 and 17, free surface and bubble interface are both plotted against time for the cases without surface tension effect and with surface tension being taken into account, respectively. It can be clearly

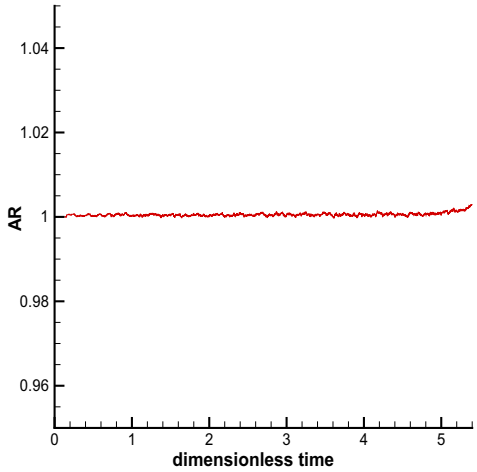

Fig. 20. The plot of the predicted area ratio (AR) against the dimensionless time for the bubble rising problem considered in [19]. Note that AR is defined as $\mathrm{AR} = \frac{\int \Phi(x,y;\ \text{for } 0.5 \leqslant \Phi \leqslant 1, t)dA}{\int \Phi(x,y;\ \text{for } 0.5 \leqslant \Phi \leqslant 1, t=0)dA}$.

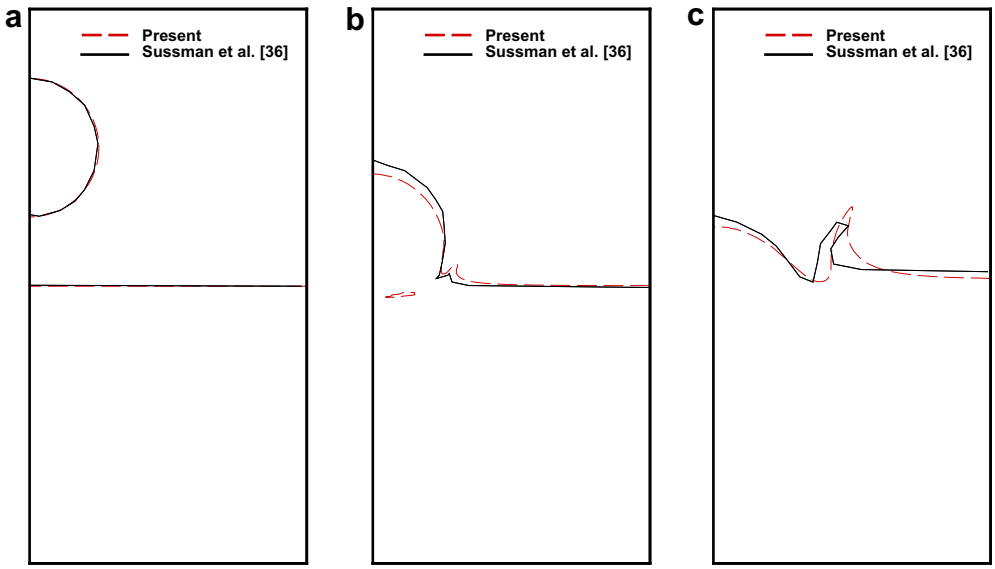

Fig. 21. Comparison of the predicted interfaces with those of Sussman et al. [36] for the droplet problem investigated in 257×257 grids. The diffusion coefficient is prescribed by $\bar{\mu} = \Delta x$. (a) $t = 0.0$; (b) $t = 2.4$; (c) $t = 3.5$.

shown that the presently predicted interface topologies agree fairly with those predicted by Zhao et al. [35]. To check the conservative property, the relative change of bubble is plotted against time in Fig. 18. As the former test problem, the bubble area is excellently preserved.

We have also conducted the analysis with the physical density ratio of 1000, considered by Sussman et al. [19], to simulate the bubble rising problem. The predicted time–evolving free surfaces and bubble interfaces, obtained in 144×144 grids with $Re = 100$ and $We = 200$, are plotted in Fig. 19. Good area-preserving feature is also demonstrated in Fig. 20.

7.3. Water droplet falling problem

We also investigate a water droplet falling through the air and hitting the originally planar free surface. The dimensionless physical properties under current investigation are set to be the same as those given in Sussman et al. [36], namely, $\mu_1 = 1$, $\mu_2 = 0.0141$, $\rho_1 = 1$, $\rho_2 = 0.00123$. The drop is initially accelerated with a fictitious gravitational force $1/Fr^2$=1/2 for a total dimensionless time of 2. Afterwards, three dimensionless parameters for characterizing the flow motion are chosen as $Re = 3518$, $Fr = 1633$ and $We = 220$, where the characteristic length and velocity are chosen as 10^{-3} m and 4 m/s, respectively. All the calculations will be carried out at $\Delta x = \Delta y = 0.03125$ and $\Delta t = 5.0 \times 10^{-4}$ for the droplet with the dimensionless radius of 1.

For the sake of enlightening the effect of surface tension, the case with consideration of surface tension is investigated for studying the interaction between the water droplet and the originally stationary water bounded by the free surface. The pre-

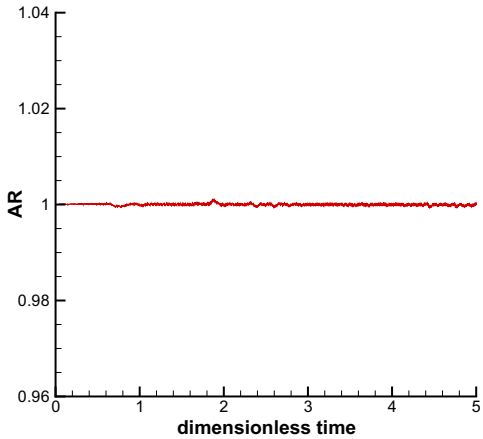

Fig. 22. The predicted area ratio (AR) against the time for the droplet problem carried out in a domain of 257×257 grids. Note that AR is defined as $\mathrm{AR} = \frac{\int \Phi(x,y;\ \text{for}\ 0.5 \leqslant \Phi \leqslant 1, t)dA}{\int \Phi(x,y;\ \text{for}\ 0.5 \leqslant \Phi \leqslant 1, t=0)dA}$.

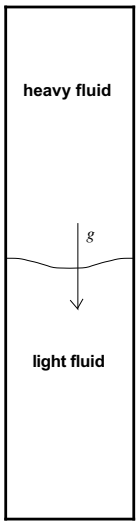

Fig. 23. Schematic of the initial condition for the Rayleigh–Taylor instability problem investigated in Section 7.4.

dicted time–evolving droplet interface and free surface in Fig. 21, plotted at the dimensionless times $t = 0.0$, $t = 2.4$ and $t = 3.5$, are compared with those given in Sussman et al. [36]. As Fig. 22 shows, the area-preserving feature remains also quite well for the case with consideration of surface tension.

7.4. Rayleigh–Taylor problem

Flow instability of the Rayleigh–Taylor type is associated with the penetration of a heavy fluid into a light fluid in the direction of gravity and has been observed in a wide range of many scientific and environmental fields. Such a Rayleigh–Taylor instability phenomenon has, therefore, been intensively studied [37]. Due to its practical and scientific importance, two incompressible fluids with the densities given by $\rho_h = 1.225\ \mathrm{kg/m^3}$ and $\rho_l = 0.1694\ \mathrm{kg/m^3}$ will be simulated in the rectangle $0 \leqslant x \leqslant 1\ \mathrm{m},\ 0 \leqslant y \leqslant 4\ \mathrm{m}$. The viscosity of the two investigated fluids, initially separated by the interface given by $y(x) = (2 + 0.1\cos(2\pi x))\ \mathrm{m}$ schematic in Fig. 23, is kept to be the same with the values of $\mu_h = \mu_l = 3.13 \times 10^{-3}\ \mathrm{kg/(m\ s)}$ in the whole domain. Like the referenced papers of Puckett et al. [38] and Popinet and Zaleski [39], flow simulation without considering surface tension will be carried out for a fluid flow starting from rest in the domain, where free slip boundary condition and non-slip boundary condition will be applied at the two vertical walls and at the horizontal top/bottom walls, respectively.

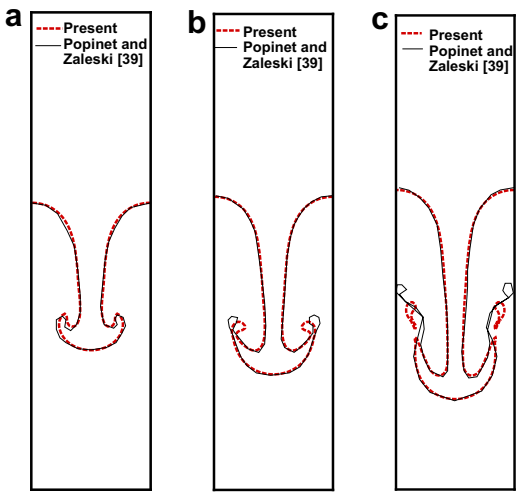

Fig. 24. Comparison of the predicted interfaces with those of Popinet and Zaleski [39] for the Rayleigh–Taylor instability problem investigated in 65×257 grids. The diffusion coefficient is prescribed by $\bar{\mu} = \Delta x$. (a) $t = 0.7$; (b) $t = 0.8$; (c) $t = 0.9$.

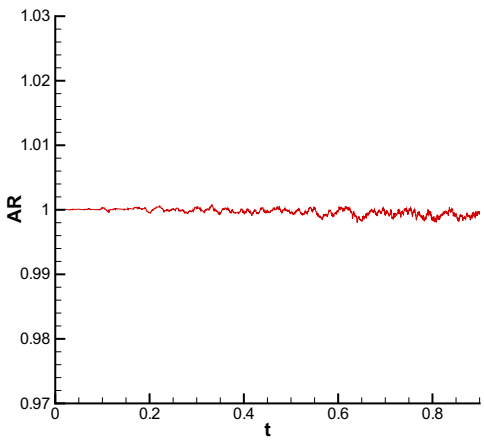

Fig. 25. The predicted area ratio (AR) against time for the Rayleigh–Taylor instability problem carried out in a domain of 65×257 grids. Note that AR is defined as $\mathrm{AR} = \frac{\int \Phi(x,y;\ \text{for}\ 0.5 \leqslant \Phi \leqslant 1, t)dA}{\int \Phi(x,y;\ \text{for}\ 0.5 \leqslant \Phi \leqslant 1, t=0)dA}$.

It can be seen from Fig. 24, which plots the development of interfaces against time at $t = 0.7$ s, 0.8 s and 0.9 s. The interface was found to be rolled up along the sides of the spike as the heavy fluid keeps penetrating into the light fluid. Development of a mushroom-type spike is a strong indication of the formation of Kelvin–Helmholtz instability due to the developed short wavelength perturbations present along the interface and parallel to the bulk flow. For the sake of comparison, we also plot the front-tracking solutions of Popinet and Zaleski [39]. It can be seen from Fig. 24 that the predicted level set solution compares favorably with other numerical predictions. Area of one fluid can be preserved quite well as Fig. 25 shows.

Moreover, another Rayleigh–Taylor problem due to Ding et al. [8] is considered. The interface is given by $y(x) = (2d + 0.1d\cos(2\pi x/d))$ in the rectangular domain $[0, d] \times [0, 4d]$, where $d = 1$. The Reynolds number under investigation is 3000. The density difference is represented by the *Atwoodratio* $At = (\rho_A - \rho_B/\rho_A + \rho_B) = 0.5$ and the viscosity ratio is 1.

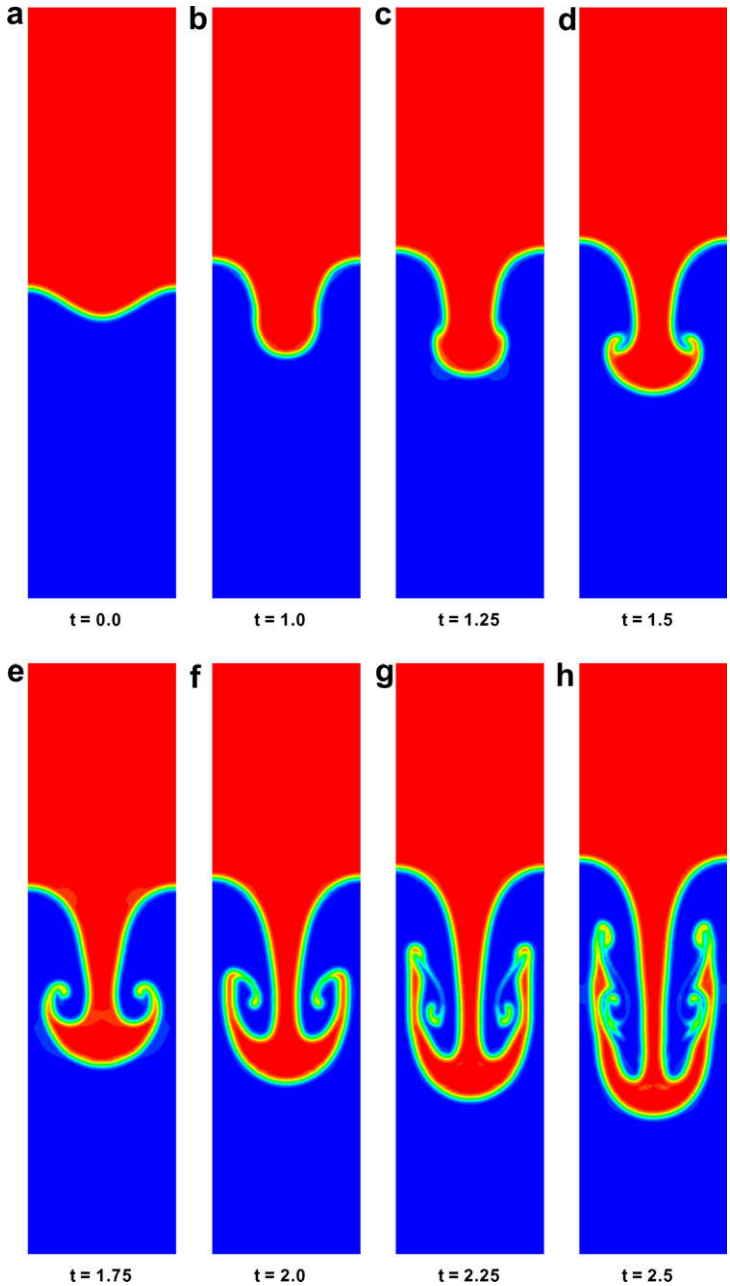

Fig. 26. The predicted time-evolving free surfaces and bubble interfaces, obtained at 80×320 grids, for the problem with $Re = 3000$ at (a) $t = 0.0$; (b) $t = 1.0$; (c) $t = 1.25$; (d) $t = 1.5$ (e) $t = 1.75$; (f) $t = 2.0$; (g) $t = 2.25$; (h) $t = 2.5$.

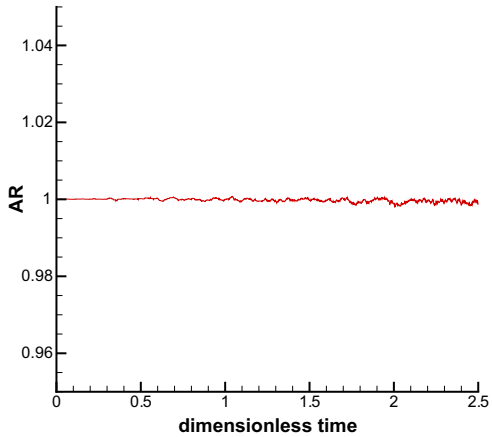

Fig. 27. Plot of the presently predicted area ratio (AR) against the dimensionless time for the Rayleigh–Taylor problem given in [8]. Note that AR is defined as $\mathrm{AR} = \frac{\int \Phi(x,y;\ \text{for}\ 0.5 \leqslant \Phi \leqslant 1, t)dA}{\int \Phi(x,y;\ \text{for}\ 0.5 \leqslant \Phi \leqslant 1, t=0)dA}$.

The predicted results for this test problem are given in Fig. 26 and in Fig. 27 for justifying the area-preserving feature from the predicted time–evolving values of AR.

8. Concluding remarks

A dispersion-relation-preserving advection scheme for modelling the incompressible two-phase flow in two dimensions by conservative level set method is formulated in non-staggered grids. The differential equation employed to model the evolving interface should accommodate the conservative interface property. This underlying transport equation should also have the ability to compress the level set function and can, therefore, sharpen the interface. Under these requirements, the nonlinear inviscid Burgers' equation cast in the transformed coordinate $\underline{\xi}(\equiv \underline{x} - \underline{u}t)$ is the underlying equation used for the numerical advection of interface with the ability to conserve the area of each phase of the fluid and to sharpen the interface. For the stabilization reason, an artificial viscosity that is sufficient to suppress the oscillations in the vicinity of interface, at which a fairly high gradient solution may be present, is explicitly added to the formulation. The derived conservative level set method will be split into the conventional level set method for the advection of the level set function and the other inhomogeneous equation, with the compressive flux and source terms being nonlinear with respect to the level set function, for compressing the interface profile. The finite volume advection scheme implemented in the advection step of the conservative level set method should yield a predicted solution that is dispersively very accurate. Both of the proposed DRP advection scheme and compact pressure gradient scheme applied in non-staggered grids have been verified analytically. Also, four benchmark problems with/without consideration of surface tension have been numerically investigated. All the predicted results have been shown to compare fairly well with the experimental and other numerical results.

Acknowledgment

This work was supported by the National Science Council of the Republic of China under Grants NSC-94-2611-E-002-021 and NSC-94-2745-P-002-002.

References

[1] J.A. Sethian, David Adalsteinsson, An overview of level set methods for etching, deposition and lithography development, IEEE Trans. Semiconduct. Manuf. 10 (1) (1997) 167–184.
[2] C.R. Anderson, A vortex method for flows with slight density variations, J. Comput. Phys. 61 (3) (1985) 417–444.
[3] J.M. Boultone-Stone, J.R. Blake, Gas bubbles bursting at a free surface, J. Fluid Mech. 254 (1993) 437–466.
[4] C.W. Hirt, B.D. Nichols, Volume of fluid method (VOF) for the dynamics of free boundaries, J. Comput. Phys. 39 (1981) 201–225.
[5] S. Unverdi, G. Tryggvason, A front-tracking method for viscous, incompressible, multi-fluid flows, J. Comput. Phys. 100 (1992) 25–37.
[6] V.E. Badalassi, H.D. Ceniceros, S. Banerjee, Computation of multiphase systems with phase field models, J. Comput. Phys. 190 (2003) 371–397.
[7] Junseok Kim, A continuous surface tension force formulation for diffuse-interface models, J. Comput. Phys. 204 (2005) 784–804.
[8] H. Ding, P.D.M. Spelt, C. Shu, Diffuse interface model for incompressible two-phase flows with large density ratios, J. Comput. Phys. 226 (2007) 2078–2095.
[9] J.A. Sethian, Peter Smereka, Level set methods for fluid interfaces, Annu. Rev. Fluid Mech. 35 (2003) 341–372.
[10] S.V. Shepel, B.L. Smith, New finite-element/finite-volume level set formulation for modelling two-phase incompressible flows, J. Comput. Phys. 218 (2006) 479–494.
[11] R. Scardovelli, S. Zaleski, Direct numerical simulation of free-surface and interfacial flow, Annu. Rev. Fluid Mech. 31 (1999) 567–603.
[12] Elin Olsson, Gunilla Kreiss, A conservative level set method for two phase flow, J. Comput. Phys. 210 (2005) 225–246.

[13] S. Osher, J.A. Sethian, Fronts propagating with curvature dependent speed: algorithms based on Hamilton–Jacobi formulation, J. Comput. Phys. 79 (1988) 12–49.
[14] P.D. Thomas, C.K. Lombard, Geometric conservation law and its application to flow computations on moving grids, AIAA J. 17 (10) (1979) 1030–1037.
[15] W.H. Sheu, Y.H. Chen, Numerical study of flow field induced by a locomotive fish in the moving meshes, Int. J. Numer. Methods Eng. 69 (2007) 2247–2263.
[16] Elin Olsson, Gunilla Kreiss, Sara Zahedi, A conservative level set method for two phase flow II, J. Comput. Phys. 225 (2007) 785–807.
[17] S. Osher, R. Fedkiw, Level Set Methods and Dynamic Implicit Surfaces, Springer-Verlag, Berlin, 2003.
[18] J.A. Sethian, Level Set Methods and Fast Marching Method, Cambridge University Press, Cambridge, 2003.
[19] M. Sussman, P. Smereka, S. Osher, A level set approach for computing solution to incompressible two-phase flow, J. Comput. Phys. 114 (1994) 146–159.
[20] A.k. Tornberg, B. Enhquist, A finite element based level set method for multiphase flow applications, Comput. Visual. Sci. 3 (2000) 93–101.
[21] M. Sussman, E.G. Puckett, A coupled level set and volume-of-fluid method for computing 3D and axisymmetric incompressible two-phase flows, J. Comput. Phys. 162 (2000) 301–337.
[22] D. Enright, R. Fedkiw, J. Ferziger, I. Mitchell, A hybrid particle level set method for improved interface capturing, J. Comput. Phys. 183 (2002) 83–116.
[23] Chirstophe Bogry, Christophe Bailly, A family of low dispersive and low dissipative explicit schemes for flow and noise computations, J. Comput. Phys. 194 (2004) 194–214.
[24] C.K.W. Tam, J.C. Webb, Dispersion-relation-preserving finite difference schemes for computational acoustics, J. Comput. Phys. 107 (1993) 262–281.
[25] I.A. Abalakin, A.V. Alexandrov, V.G. Bobkov, T.K. Kozubskaya, High accuracy methods and software development in computational aeroacoustics, J. Comput. Methods Sci. Eng. 2 (2003) 1–14.
[26] O.A. Ladyzhenskaya, The Mathematical Theory of Viscous Incompressible Flow, Gordon and Breach, New York, 1969.
[27] P. Lin, A sequential regularization method for time-dependent incompressible Navier–Stokes equations, SIAM J. Numer. Anal. 34 (1997) 1051–1071.
[28] Tony W.H. Sheu, R.K. Lin, An incompressible Navier–Stokes model implemented on non-staggered grids, Numer. Heat Trans., B Fundam. 44 (2003) 277–294.
[29] J.E. Pilliod, E.G. Puckett, Second-order accurate volume-of-fluid algorithms for tracking material interface, J. Comput. Phys. 199 (2004) 465–502.
[30] U. Ghia, K.N. Ghia, C.T. Shin, High-Re solutions for incompressible flow using the Navier–Stokes equations and a multigrid method, J. Comput. Phys. 48 (1982) 387–411.
[31] J. Martin, W. Moyce, An experimental study of the collapse of liquid columns on a rigid horizontal plane, Philos. Trans. 244 (1952) 312–324.
[32] F.J. Kelecy, R.H. Pletcher, The development of a free surface capturing approach for multidimensional free surface flows in closed containers, J. Comput. Phys. 138 (1997) 939–980.
[33] J.G. Hnat, J.D. Buckmaster, Spherical cap bubbles and shirt formation, Phys. Fluids 19 (1976) 182–194.
[34] D. Bhaga, M.E. Weber, Bubbles in viscous liquids: shapes, wakes, and velocities, J. Fluid Mech. 105 (1981) 61–85.
[35] Y. Zhao, H.H. Tan, B. Zhang, A high-resolution characteristics-based implicit dual time-stepping VOF method for free surface flow simulation on unstructured grids, J. Comput. Phys. 183 (2002) 233–273.
[36] M. Sussman, A.S. Almgren, J.B. Bell, P. Colella, L.H. Howell, M.L. Welcome, An adaptive level set approach for incompressible two-phase flows, J. Comput. Phys. 148 (1999) 81–124.
[37] Anton Smolianski, Finite-element/level-set/operator-splitting (FELSOS) approach for computing two-fluid unsteady flows with free moving interfaces, Int. J. Numer. Methods Fluids 48 (2005) 231–269.
[38] E.G. Puckett, A.S. Almgren, J.B. Bell, D.L. Marcus, W.J. Rider, A high-order projection method for tracking fluid interfaces in variable density incompressible flows, J. Comput. Phys. 130 (1997) 269–282.
[39] S. Popinet, S. Zaleski, A front-tracking algorithm for accurate representation of surface tension, Int. J. Numer. Methods Fluids 30 (1999) 775–793.